Monthly Notices
of the
ROYAL ASTRONOMICAL SOCIETY

MNRAS **489,** 3810–3826 (2019)
Advance Access publication 2019 August 30

doi:10.1093/mnras/stz2383

Timing of young radio pulsars – I. Timing noise, periodic modulation, and proper motion

A. Parthasarathy [1,2,3★] R. M. Shannon,[1,2] S. Johnston [3] L. Lentati,[4] M. Bailes,[1,2] S. Dai,[3] M. Kerr [5] R. N. Manchester,[3] S. Osłowski [1,2] C. Sobey [6] W. van Straten [7] and P. Weltevrede [8]

[1]*Centre for Astrophysics and Supercomputing, Swinburne University of Technology, PO Box 218, Hawthorn, VIC 3122, Australia*
[2]*OzGrav: Australian Research Council Centre of Excellence for Gravitational Wave Discovery, Swinburne University of Technology, Mail number H74, PO Box 218, Melbourne, VIC 3122, Australia*
[3]*CSIRO Astronomy and Space Science, Australia Telescope National Facility, PO Box 76, Epping, NSW 1710, Australia*
[4]*Astrophysics Group, Cavendish Laboratory, JJ Thomson Avenue, Cambridge CB3 0HE, UK*
[5]*Space Science Division, Naval Research Laboratory, Washington, DC 20375, USA*
[6]*CSIRO Astronomy and Space Science, PO Box 1130, Bentley, WA 6102, Australia*
[7]*Institute for Radio Astronomy & Space Research, Auckland University of Technology, Private Bag 92006, Auckland 1142, New Zealand*
[8]*Jodrell Bank Centre for Astrophysics, The University of Manchester, Alan Turing Building, Manchester M13 9PL, UK*

Accepted 2019 August 23. Received 2019 August 22; in original form 2019 March 23

ABSTRACT

The smooth spin-down of young pulsars is perturbed by two non-deterministic phenomenon, glitches, and timing noise. Although the timing noise provides insights into nuclear and plasma physics at extreme densities, it acts as a barrier to high-precision pulsar timing experiments. An improved methodology based on the Bayesian inference is developed to simultaneously model the stochastic and deterministic parameters for a sample of 85 high-$\dot{E}$ radio pulsars observed for ∼10 yr with the 64-m Parkes radio telescope. Timing noise is known to be a red process and we develop a parametrization based on the red-noise amplitude ($A_{\rm red}$) and spectral index (β). We measure the median $A_{\rm red}$ to be $-10.4^{+1.8}_{-1.7}$ yr$^{3/2}$ and β to be $-5.2^{+3.0}_{-3.8}$ and show that the strength of timing noise scales proportionally to $\nu^{1}|\dot{\nu}|^{-0.6\pm0.1}$, where ν is the spin frequency of the pulsar and $\dot{\nu}$ is its spin-down rate. Finally, we measure significant braking indices for 19 pulsars and proper motions for 2 pulsars, and discuss the presence of periodic modulation in the arrival times of 5 pulsars.

Key words: methods: data analysis – stars: neutron – pulsars: general.

1 INTRODUCTION

Young neutron stars provide unique insights into astrophysics, which are not available from the bulk of the pulsar population. They frequently exhibit two types of deviations from a steady spin-down behaviour, 'glitches', and 'timing noise'. Glitches are sudden jumps in the pulsars' spin frequency acting as probes of neutron star interiors. Timing noise is a type of rotational irregularity that causes the pulse arrival times to stochastically wander about a steady spin-down state. Our sample is a representative of pulsars that are spinning down rapidly and present the most promising avenue for detailed studies of timing noise, glitches, and their spin-down behaviour.

The technique of pulsar timing enables the precise measurement of their spin periods (P) and their spin-down rates ($\dot{P}$), allowing us to study their evolution in the P–$\dot{P}$ diagram (Johnston & Karastergiou 2017; see fig. 1). Although young pulsar timing offers several opportunities to explore a plethora of astrophysical phenomena, it is a challenging prospect as most of these astrophysical signals are dominated or biased by timing noise and glitches. A careful methodology is thus needed in the analysis of young pulsar timing data to disentangle the deterministic processes from the stochastic components. For example, young pulsars are thought to be associated with supernova remnants, and measuring their proper motions (Hobbs et al. 2005) allows us to probe the connections between the neutron star and its progenitor, which has implications for birth rate statistics (Manchester 2004). Unbiased measurements of proper motion through pulsar timing can be obtained only if the timing noise in the pulse arrival times is modelled accurately. While understanding the origin of the stochastic signals present in the time of arrivals (ToAs) is important, it is also essential to

★ E-mail: adityapartha3112@gmail.com (AP); rshannon@swin.edu.au (RMS); simon.johnston@atnf.csiro.au (SJ)

characterize and mitigate the effects of these signals as part of the general timing model because it reduces the bias in the estimation of other deterministic pulsar parameters.

1.1 Timing noise

Timing noise manifests itself as a red-noise process in the ToAs, implying an autocorrelated process on a time-scale of months to years and is generally described by a wide-sense stationary stochastic signal (Groth 1975). Boynton et al. (1972) attempted to describe the timing noise in the Crab pulsar as random walks in either the phase, frequency, or the spin-down parameter of the pulsar. They showed that the power spectra expected from such random walks will be proportional to −2, −4, and −6 for phase, frequency, and spin-down, respectively. Following this, many attempts have been made to study the timing noise in pulsars over increasing data spans and for a larger sample of pulsars. Cordes & Helfand (1980) studied the timing behaviour of 50 pulsars and found that the timing activity was correlated with $\dot{P}$ but weakly correlated with P and concluded that timing activity is consistent with a random walk origin. As more pulsars with longer data sets were studied, it became apparent that timing noise might be explained by a combination of different random walks in pulsar spin frequency (ν) and spin-frequency derivative ($\dot{\nu}$) and by discrete jumps in phase and spin parameters. Timing noise is thought to arise due to changes in the coupling between the neutron star crust and its superfluid core (Jones 1990) or magnetospheric torque fluctuations (Cheng 1987b; Lyne et al. 2010). It has also been attributed to microjumps, which are similar to small glitches (Melatos, Peralta & Wyithe 2008) and fluctuations in the spin-down torque (Cheng 1987a). It has often been suggested that the superfluid interior of a neutron star can have macroscopic Kolmogorov-like turbulence that can contribute to stochasticity in the spin-down processes observed in radio pulsars (Greenstein 1970; Link 2012; Melatos & Link 2014).

The observations of quasi-periodic state switching of pulsars (Kramer et al. 2006; Lyne et al. 2010), each state with a distinct spin-down rate, led to alternative descriptions of timing noise being periodic or quasi-periodic processes. Unmodelled planetary companions (Kerr et al. 2015), pulse-shape changes (Brook et al. 2016), accretion from the interstellar medium (Cordes & Greenstein 1981), or free precession (Stairs, Lyne & Shemar 2000; Kerr et al. 2016) have also been attributed as explanations for the observed low-frequency structures in the ToAs. Hobbs et al. (2005) studied a large sample of pulsars observed over ∼10 yr and concluded that timing noise is widespread in pulsars and it cannot be explained as a simple random walk in pulse phase, frequency, or spin-down rate. The timing noise in millisecond pulsars (MSPs) has been mainly studied to understand their sensitivity to nHz-frequency gravitational waves (Caballero et al. 2016; Lentati et al. 2016; Lam et al. 2017). However, unlike MSPs, the timing noise in young pulsars is very strong, often contributing many cycles of pulse phase on week to month time-scales. Shannon & Cordes (2010) pointed out that the observed strength of timing noise varies by more than eight orders of magnitude over magnetars, young, and MSPs.

1.2 Pulsar spin-down and braking index

The long-term spin-down of a pulsar can be approximated as

$$\dot{\nu} = -K\nu^n, \tag{1}$$

where K is a constant and n is the braking index. The braking index describes the relationship between the braking torque acting on a pulsar and its spin-frequency parameters, and provides a probe into the physics dictating pulsar temporal evolution. We solve for n by taking the derivative of equation (1),

$$n = \frac{\nu\ddot{\nu}}{\dot{\nu}^2}, \tag{2}$$

where $\ddot{\nu}$ is the second derivative of the spin frequency. For standard magnetic-dipole braking, the magnetic field strength and the magnetic-dipole inclination angle are assumed to be constant in time, with $n = 3$ (Espinoza, Lyne & Stappers 2017). While measuring ν and $\dot{\nu}$ is trivial using standard timing methods, measuring the long-term $\ddot{\nu}$ is challenging, mainly because of the fact that it is a very small quantity. In 'old' pulsars, with $\nu \sim 1$ Hz and $\dot{\nu} \sim 10^{-15}$ Hz s^{-1}, the estimated $\ddot{\nu}$ from equation (2) is $\sim 10^{-30}$ Hz s^{-2}. However for the youngest pulsars we estimate $\ddot{\nu}$ to be $< 10^{-20}$ Hz s^{-2}, which makes these pulsars suitable for studying pulsar braking mechanisms (Johnston & Galloway 2000). If both K and n are constant in time, a pulsar will follow a track in the P–$\dot{P}$ diagram with a slope of $2 - n$. The P–$\dot{P}$ diagram can then be used as an evolutionary tool in which pulsars are born in the upper left region, and as they age and spin-down they drift towards the cluster of 'normal' pulsars, with periods of ∼0.5 s (Johnston & Karastergiou 2017).

Both timing noise and glitches introduce variations in $\dot{\nu}$ which becomes problematical in the long-term measurement of $\ddot{\nu}$. Glitches are often modelled as permanent changes in spin frequency (ν) and spin-frequency derivative ($\dot{\nu}$) or as exponential decays in ν over τ days and are typically attributed to either the transfer of angular momentum between the superfluid interior and the solid crust of the neutron star (Anderson & Itoh 1975; Alpar, Nandkumar & Pines 1985) or as star quakes in the crystalline outer crust of the neutron star (Ruderman 1969).

1.3 Quasi-periodic modulations

The reflex motion resulting from the orbital motion of a companion to a pulsar, introduces modulations in the ToAs, which led to e.g. the discovery of the double neutron star system B1913+16 (Hulse & Taylor 1975) and the first exoplanets (Wolszczan & Frail 1992). Precession induces a periodic change in the spin-down torque which causes ToA modulation and since our line of sight cuts across different parts of the neutron star polar cap, there can also be an observed change in the shape of the pulse profile (Link & Epstein 2001). Such events of ToA modulations were reported by Lyne et al. (2010) in 17 pulsars, of which 6 showed correlations with pulse profile variations. Recently, Stairs et al. (2019) reported correlated shape and spin-down changes in PSR J1830–1059, which they attributed to large-scale magnetospheric switching. Brook et al. (2016) analysed 168 pulsars and searched for correlations between profile shape changes and $\dot{\nu}$ and found that although this correlation is clear in some pulsars, the intrinsic relationship between change in $\dot{\nu}$ and profile variability may be much more complex than previously postulated (see also Kerr et al. 2016).

1.4 Proper motions

Pulsars are created in supernovae, and the birth process is expected to impart a high 'kick velocity'. Various mechanisms have been proposed for these kicks, including an asymmetric neutrino emission in the presence of superstrong magnetic fields (Lai & Qian

1998), a post-natal electromagnetic rocket mechanism (Harrison & Tademaru 1975), asymmetric explosion of γ-ray bursts (Cui et al. 2007), and hydrodynamical instabilities in the collapsed supernova core (Lai & Goldreich 2000). While the evidence for such kicks is unequivocal (Johnston et al. 2005), their physical origin remains unclear. A pulsar's proper motion causes sinusoidal variations in ToAs with a periodicity of 1 yr and an amplitude which increases with time.

1.5 The Bayesian pulsar timing framework

Lentati et al. (2013) pointed out that in order to obtain an unbiased estimation of the pulsar parameters (proper motions, spin parameters, braking index etc.) it is important to simultaneously model the stochastic (timing noise) and the deterministic (pulsar) parameters. Most of the frequentist approaches (Hobbs et al. 2004; Coles et al. 2011) do not consider the covariances between the timing model and the stochastic processes, and the uncertainties in the parameter estimates, motivating the development of TEMPONEST (Lentati et al. 2014), which performs a simultaneous analysis of the timing model and additional stochastic parameters using the Bayesian inference tool, MULTINEST (Feroz, Hobson & Bridges 2009; Feroz, Hobson & Bridges 2011). It also allows for robust model selection between different sets of timing parameters based on the Bayesian evidences. We use TEMPONEST to simultaneously model the pulsar parameters and the noise parameters and use the Bayesian evidence to select the optimal model for each pulsar. Such an analysis allows us to discuss the statistical properties of timing noise and also compare the results with those obtained from other Bayesian tools.

In Section 2, we describe the observing program and the data processing pipeline. In Section 3, we describe the Bayesian timing analysis in detail and present the mathematical formulation of the timing model. In Section 4, we present the basic observational characteristics, the timing solutions, the timing noise models for our sample of pulsars along with the new proper motions. Finally in Section 5, we delve into the implications of our results.

2 OBSERVATIONS

In this paper, we study 85 pulsars observed at a monthly cadence using the 64-m CSIRO Parkes radio telescope in support of the *Fermi* mission that commenced in 2007 February (Smith et al. 2008; Weltevrede et al. 2010). We selected pulsars for which there were no identified glitches.[1] These pulsars have $\dot{E} > 10^{34}$ erg s^{-1}, surface magnetic fields typically ranging from 10^{12} to 10^{13} G with characteristic ages of 10^5–10^6 yr as shown in Fig. 1. Two pulsars, PSR J1513–5908 and J1632–4818 have known associations with supernova remnants, five other pulsars, PSR J0543+2329, J1224–6407, J1509–5850, J1809–1917, J1833–0827 are known XRS and 3 others, J1509–5850, J1513–5908, J1648–4611 are known GRS (Abdo et al. 2013).

Most of these observations were carried out using the 20-cm multibeam receiver (Staveley-Smith et al. 1996), with 256 MHz of bandwidth divided into 1024 frequency channels and folded in real time into 1024 phase bins. Some of these pulsars were also observed at radio wavelengths of 10 and 40 cm. Each pulsar is observed for a few minutes depending upon its flux density. The observations were excised of radio frequency interference (RFI) and calibrated

[1]In subsequent analysis described below, two relatively small glitches were detected and parametrized.

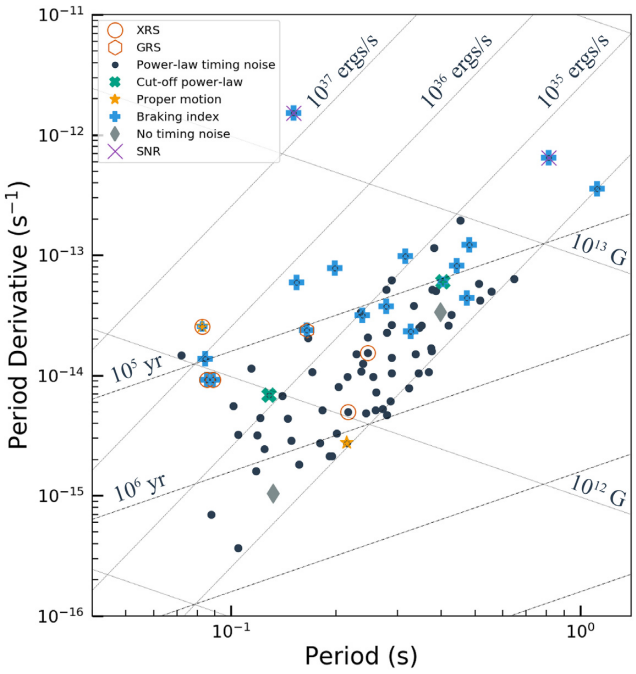

Figure 1. The P–$\dot{P}$ diagram showing our sample of 85 young pulsars coloured according to their preferred timing model. The different timing models are outlined in Section 3. A few pulsars are also highlighted to be X-ray (XRS) or gamma-ray sources (GRS) and/or to have known supernova associations (SNR). Our sample of pulsars mostly have $\dot{E} > 10^{34}$ erg s^{-1} and surface magnetic fields ranging from 10^{12} to 10^{13} G with characteristic ages of 10^5–10^6 yr.

using standard PSRCHIVE (Hotan, van Straten & Manchester 2004) tools and averaged in frequency, time, and polarization. The ToAs of the pulses were computed by correlating a high signal-to-noise ratio, smoothed template with the averaged observations. For this analysis, we use only the 20-cm observations as the 10-cm data are sparsely spaced in time and the 50-cm data are highly corrupted by RFI.

3 TIMING ANALYSIS

Establishing a phase coherent solution to the ToAs is an important step in the process of pulsar timing. We know that most of the young pulsars have a strong presence of timing noise and frequent glitches, which makes it difficult to produce and maintain phase-connected timing solutions. We use the pulsar-timing code, TEMPO2 (Hobbs, Edwards & Manchester 2006) to attribute relative pulse numbers to the ToAs and obtain phase connection in the timing residuals.

We split the timing analysis into two steps. The first step involves phase connecting the timing residuals. The second step involves using the phase connected timing solution in the Bayesian timing package, TEMPONEST, to construct a complete timing model with stochastic and additional deterministic parameters. TEMPONEST allows us to simultaneously model stochastic and deterministic parameters of interest and marginalize over nuisance parameters that are of no interest to this analysis. For example, in one of the timing models, we fitted the timing noise parameters (white noise and red noise) while simultaneously searching over a wide range of position and spin parameters, while keeping the dispersion measure (DM) fixed. We compute a Bayesian log-evidence value associated

with the models for each pulsar to determine which timing model is preferred.

The ToAs for each pulsar are considered to be a sum of both deterministic and stochastic components:

$$t_{\rm tot} = t_{\rm det} + t_{\rm sto}. \quad (3)$$

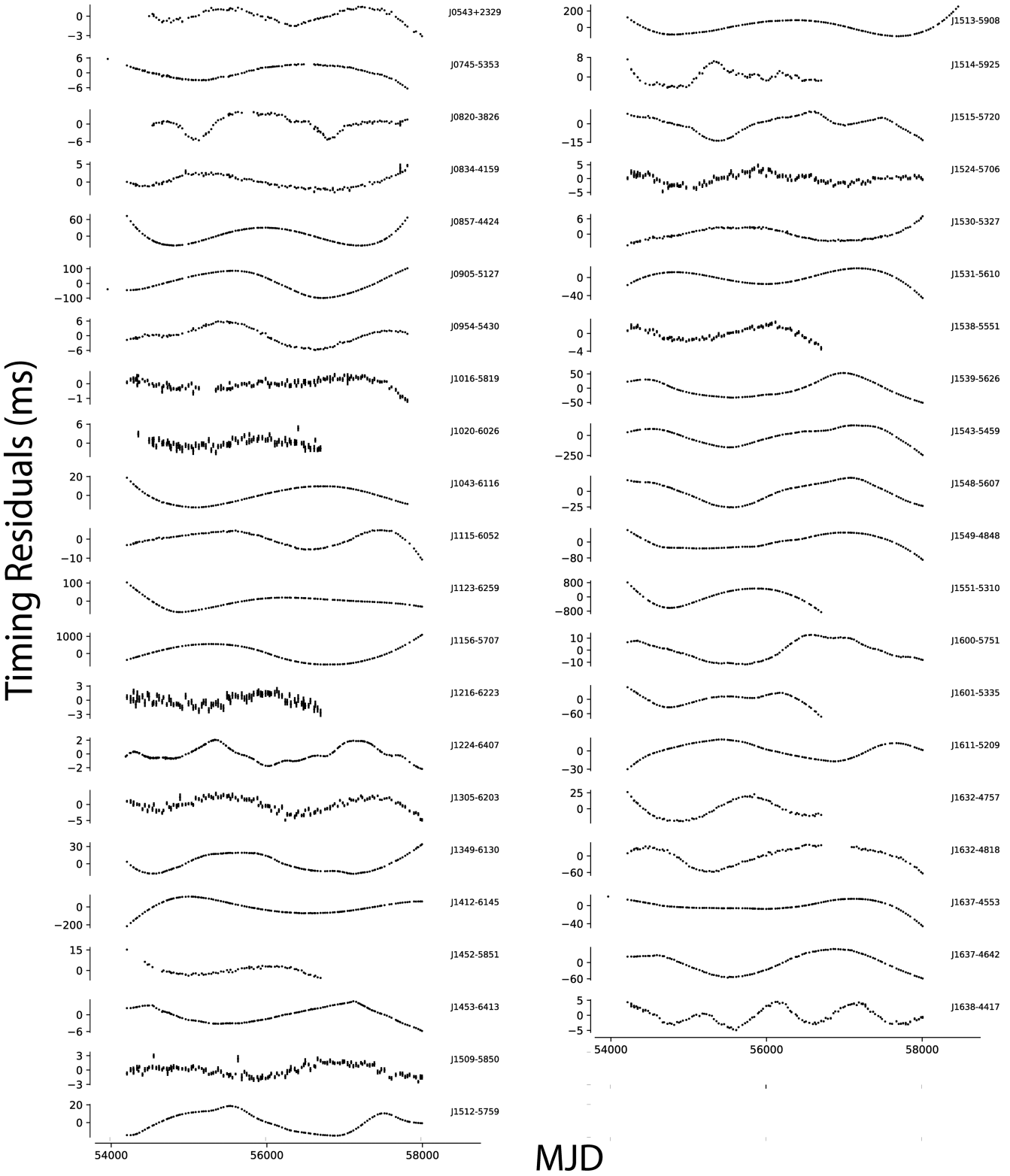

Figure 2. Phase-connected timing residuals depicting different levels of timing noise. The timing residuals from the preferred model are shown here, but without removing the contribution of the timing noise.

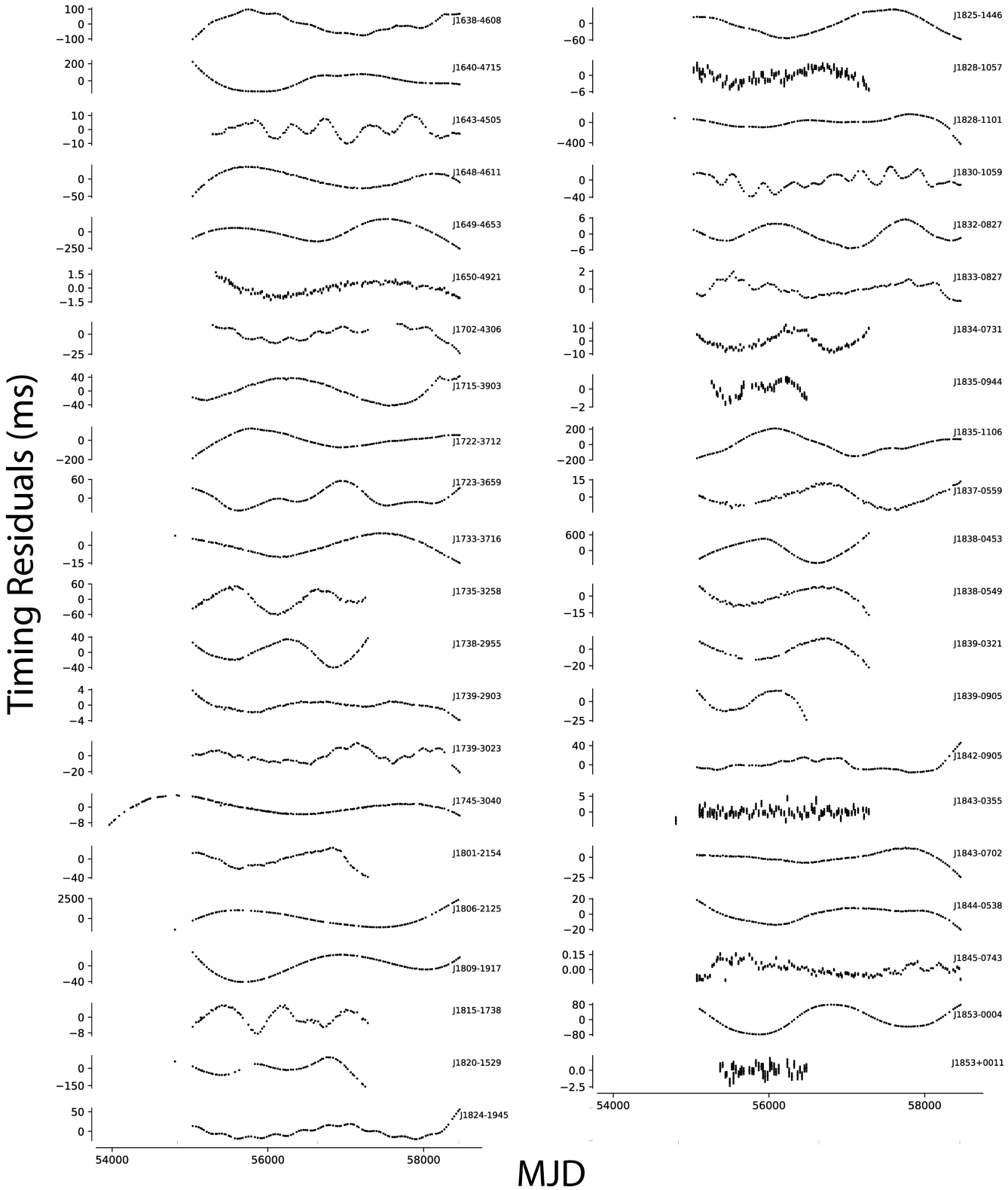

Figure 2 – continued

The deterministic components in our timing models include various permutations of the pulsar position, spin, proper motion, and the spin-down parameters while the stochastic contribution is computed by introducing additional parameters that describe the white and

red noise processes. The white noise is modelled by adjusting the uncertainty on individual ToAs to be,

$$\sigma^2 = F{\sigma_{\rm r}}^2 + {\sigma_{\rm Q}}^2, \tag{4}$$

where F, referred to as EFAC, is introduced as a free parameter to account for instrumental distortions and ${\sigma_{\rm r}}^2$ is the formal uncertainty obtained from ToA fitting. In our analysis we use a global EFAC flag for our 20-cm observations. An additional white noise component (${\sigma_{\rm Q}}^2$), commonly referred to as EQUAD, is used to model an additional source of time-independent noise measured for each observing system.

In young pulsars, radio-frequency independent timing noise is the dominant contributing factor towards the red-noise in the ToAs. Many approaches have been taken to improve the parameter estimates by removing some portion of this low-frequency timing noise. Hobbs et al. (2004) developed a technique to 'whiten' the timing residuals using harmonically related sinusoids that allowed the measurements of proper motions for a large sample of young pulsars using standard timing methods. Coles et al. (2011) argued that the previously developed 'pre-whitening' methods assumed that the measurements were uncorrelated which resulted in a bias in the parameter estimates. They proposed a new method of improving the timing model fit by using the Cholesky decomposition of the covariance matrix, which described the stochastic processes in the ToAs. They argued that the optimal approach to characterize timing noise, especially those dominated by the presence of strong red noise is to analyse the power spectral density of the pulsar timing residuals. They modelled the timing noise in pulsars using a power-law model to fit for an amplitude (A) and a spectral index estimate (β). This technique has been used to determine the timing noise parameters and proper motions of MSPs (Reardon et al. 2016).

van Haasteren & Levin (2013) later developed a joint analysis of the deterministic timing model and the stochastic parameters using a Markov Chain approach and argued that the stationarity of the time-correlated residuals breaks down in the fitting process and that failure to account for the covariances between the deterministic and stochastic parameters leads to incorrect estimation of the uncertainties in the spectral estimates, especially for quadratic spin-down parameters. However, Lentati et al. (2013) pointed out that because the parameter space changes with the linearization of the timing model, it becomes difficult to perform model selection with the approach in van Haasteren & Levin (2013).

In our analysis we do not search for DM variations and fix the value for the DM in all the models. This is justified as Petroff et al. (2013) found only upper limits to DM variations in the pulsars under consideration here. We model the timing noise as a power-law power spectrum characterized with a red-noise amplitude ($A_{\rm red}$) and a spectral index (β):

$$P_{\rm r}(f) = \frac{A_{\rm red}^2}{12\pi^2}\left(\frac{f}{f_{\rm yr}}\right)^{-\beta}, \tag{5}$$

where $f_{\rm yr}$ is a reference frequency of 1 cycle per year and $A_{\rm red}$ is in units of yr$^{3/2}$.

Motivated by the observations of quasi-periodic timing noise observed in many pulsars, we also model the timing noise as a cut-off power law as described by

$$P_{\rm r,CF}(f) = \frac{A(f_{\rm c}/f_{\rm yr})^{-\beta}}{[1+(f/f_{\rm c})^{-\beta/2}]^2}, \tag{6}$$

where $f_{\rm c}$ is the corner frequency and A is ($A_{\rm red}^2/12\pi^2$). We also consider the fact that in young pulsars, the measured timing noise spectral index tends to be steeper as compared to the rest of the pulsar population, with measured values of $\beta \sim 9$ (Shannon, Johnston & Manchester 2014) and so we include low-frequency components with frequencies $f < 1/T_{\rm span}$ to model the lowest frequency timing noise.

A systematic search for periodic modulations in the ToAs is also conducted. We search for harmonic modulations by fitting for a sinusoid with an arbitrary phase, frequency, and amplitude and compare the Bayes factor of this model with the others. We also simultaneously model the stochastic parameters with the proper motion parameters to obtain a more robust estimation of the transverse velocity of the pulsar.

Finally, we search for a braking index, which is caused due to the deceleration of the spin-down rate due to the associated decrease in the magnetic torque. For young pulsars, this braking introduces a measurable second derivative of the spin frequency,

$$\ddot{\nu}_{\rm b} = n\frac{\dot{\nu}^2}{\nu}, \tag{7}$$

and potentially even a third frequency derivative,

$$\dddot{\nu}_{\rm b} = n(2n-1)\frac{\dot{\nu}^3}{\nu^2}. \tag{8}$$

Analysing the braking indices from a large sample of young pulsars offers a window into the various processes that govern the pulsar spin-down. Pulsar braking is a deterministic process and is manifested as low-frequency structures in the ToAs.

3.1 The Bayesian inference method

At the heart of all Bayesian analysis is the Bayes' theorem, which for a given set of parameters Θ in a model H, given data D, can be written as:

$$\Pr(\Theta \mid D, H) = \frac{\Pr(D \mid \Theta, H)\Pr(\Theta \mid H)}{\Pr(D \mid H)}, \tag{9}$$

where

(i) $\Pr(\Theta \| D, H) \equiv \Pr(\Theta)$ is the posterior probability distribution of the parameters,
(ii) $\Pr(D \| \Theta, H) \equiv L(\Theta)$ is the likelihood of a particular model,
(iii) $\Pr(\Theta \| H) \equiv \pi(\Theta)$ is the prior probability distribution of the parameters,
(iv) and $\Pr(D \| H) \equiv Z$ is the Bayesian evidence.

The way we discriminate one model over the other is by considering the evidence (Z) which is the factor required to normalize the posterior over Θ,

$$Z = \int L(\Theta)\pi(\Theta)\mathrm{d}^n\Theta, \tag{10}$$

where n is the dimensionality of the parameter space and the 'odds ratio', R,

$$R = \frac{Z_1}{Z_2}\frac{Pr(H_1)}{Pr(H_0)}, \tag{11}$$

where $\frac{\Pr(H_1)}{\Pr(H_0)}$ is the a priori probability ratio for the two models.

Assuming the prior probability of the two models is unity, the odds ratio R reduces to the Bayes factor which is then the probability of one model compared to the other. Since in our analysis we compute the log-evidence, the log Bayes factor is then simply the difference of the log-evidences for the two models. A model is preferred if the log Bayes factor is greater than 5. This states that with equal prior odds, we can expect there to be a $1e^{-5}$ chance, (i.e. 1 in 150) that one hypothesis is true over the other. This is similar

Table 1. Observational characteristics of the 85 pulsars described in this paper. The position and spin-down parameters are reported at the mentioned period epoch (PEPOCH) along with the time span and the MJD range. The 95 per cent confidence limits for the position and spin parameters reported here are derived from the preferred model for each pulsar. The confidence regions are individually stated, if the upper and lower confidence limits are asymmetric.

PSR	RAJ (h:m:s)	Dec.J (d:m:s)	PEPOCH	ν (s^{-1})	$\dot{\nu}$ (10^{-14} s^{-2})	$N_{\rm ToA}$	Time span (yr)	MJD range
J0543+2329	$05{:}43{:}11.26^{0.05}_{0.62}$	$23{:}16{:}39.66^{0.91}_{0.03}$	55580	4.065 310 293 96(8)	−25.483 51(13)	111	9.6	54505–58011
J0745–5353	07:45:04.48(4)	−53:53:09.56(3)	55129	4.654 659 072 22(10)	−4.738 02(14)	173	10.5	53973–57824
J0820–3826	08:20:59.929(9)	−38:26:42.9(13)	55583	8.010 466 568 02(3)	−15.6734(5)	115	9.0	54548–57824
J0834–4159	08:34:17.807(2)	−41:59:35.99(2)	55308	8.256 427 513 76(12)	−29.182 13(2)	134	9.9	54220–57824
J0857–4424	08:57:55.832(2)	−44:24:10.65(2)	55335	3.060 104 5423(4)	−19.6145(10)	170	9.9	54220–57824
J0905–5127	09:05:51.96(2)	−51:27:54.05(2)	55341	2.887 660 036 64(2)	−20.7322(6)	136	10.5	53971–57824
J0954–5430	09:54:06.046(5)	−54:30:52.82(4)	55323	2.114 833 070 64(18)	−19.6358(5)	125	9.9	54220–57824
J1016–5819	10:16:12.071(2)	−58:19:01.07(16)	55333	11.385 078 985 52(7)	−9.057 63(13)	128	9.9	54220–57824
J1020–6026	10:20:11.41(19)	−60:26:06.3(12)	55494	7.118 385 668 03(5)	−34.1421(5)	81	6.4	54365–56708
J1043–6116	10:43:55.261(2)	−61:16:50.76(2)	55358	3.464 939 984 47(4)	−12.491 69(7)	131	9.9	54220–57824
J1115–6052	11:15:53.722(4)	−60:52:18.61(3)	55366	3.849 420 365 20(10)	−10.709 96(13)	130	10.4	54220–58011
J1123–6259	11:23:55.53(12)	−62:59:10.94(8)	55393	3.684 105 494 79(18)	−7.135 60(2)	131	10.4	54220–58011
J1156–5707	11:56:07.45(7)	−57:07:02.1(6)	55354	3.467 204 7206(6)	−31.9149(9)	134	10.4	54220–58011
J1216–6223	12:16:41.96(13)	−62:23:57.00(9)	55391	2.673 417 841 032(14)	−12.024 08(14)	90	6.8	54220–56708
J1224–6407	12:24:22.254(6)	−64:07:53.87(4)	55191	4.619 368 688 62(6)	−10.569 60(8)	274	10.4	54204–58011
J1305–6203	13:05:21.14(10)	−62:03:21.07(8)	55390	2.337 684 822 03(6)	−17.573 35(10)	127	10.4	54220–58011
J1349–6130	13:49:36.62(18)	−61:30:17.12(15)	55429	3.855 573 841 97(19)	−7.606 78(3)	171	10.4	54220–58012
J1412–6145	14:12:07.63(10)	−61:45:28.48(8)	55363	3.172 000 7909(13)	−99.643(4)	162	10.4	54220–58012
J1452–5851	14:52:52.60(10)	−58:51:13.2(11)	55367	2.586 365 680 859(2)	−33.916 06(17)	75	6.8	54220–56708
J1453–6413	14:53:32.665(6)	−64:13:16.00(5)	55433	5.571 440 213 75(9)	−8.518 12(15)	184	10.4	54220–58012
J1509–5850	15:09:27.156(7)	−58:50:56.01(8)	55378	11.245 448 8757(7)	−115.9175(16)	129	10.4	54220–58012
J1512–5759	15:12:43.04(10)	−57:59:59.8(11)	55383	7.770 093 920 40(18)	−41.372 72(2)	131	10.4	54220–58012
J1513–5908	$15{:}13{:}55.81^{0.11}_{0.1}$	$-59{:}08{:}09.64^{0.04}_{0.11}$	55336	6.597 091 827 78(19)	−6653.105 58(27)	151	11.6	54220–58469
J1514–5925	15:14:59.10(3)	−59:25:43.5(3)	55415	6.720 544 472 15(8)	−13.0014(17)	85	6.8	54220–56708
J1515–5720	15:15:09.23(14)	−57:20:50.15(17)	55380	3.488 596 141 04(17)	−7.41624(2)	130	10.4	54220–58012
J1524–5706	15:24:21.42(12)	−57:06:34.64(15)	55383	0.895 917 294 63(9)	−28.603 66(2)	128	10.4	54220–58012
J1530–5327	15:30:26.892(2)	−53:27:56.02(4)	55431	3.584 763 701 33(5)	−6.01385(9)	158	10.4	54220–58012
J1531–5610	15:31:27.901(11)	−56:10:55.33(13)	55304	11.875 629 2823(4)	−194.5360(14)	140	10.4	54220–58012
J1538–5551	15:38:45.016(5)	−55:51:36.95(8)	55421	9.553 297 189 30(4)	−29.2693(6)	85	6.8	54220–56708
J1539–5626	15:39:14.06(18)	−56:26:26.3(2)	55408	4.108 545 287 47(18)	−8.183 23(2)	128	10.4	54220–58012
J1543–5459	15:43:56.43(6)	−54:59:15.0(8)	55408	2.651 550 8603(4)	−36.6285(7)	128	10.4	54220–58012
J1548–5607	15:48:44.015(8)	−56:07:34.3(10)	55408	5.850 075 804 47(19)	−36.731 72(3)	128	10.4	54220–58012
J1549–4848	15:49:21.08(17)	−48:48:35.5(3)	55407	3.467 948 675 00(2)	−16.966 93(3)	130	10.4	54220–58012
J1551–5310	15:51:41.0(10)	−53:11:00.5(4)	55383	2.205 325 738 02(11)	−94.7569(18)	84	6.8	54220–56708
J1600–5751	16:00:19.90(11)	−57:51:15.3(13)	55377	5.142 554 333 75(2)	−5.630 69(3)	129	10.4	54220–58012
J1601–5335	16:01:54.81(2)	−53:35:44.1(4)	55391	3.466 452 814 46(7)	−74.9184(10)	86	6.8	54220–56708
J1611–5209	$16{:}11{:}03.37(01)$	$-52{:}09{:}22.13^{0.1}_{0.11}$	55390	5.479 608 123 33(12)	−15.524 78(19)	128	10.4	54220–58012
J1632–4757	16:32:16.66(13)	−47:57:34.5(3)	55419	4.375 052 744 87(4)	−28.8454(7)	83	6.8	54220–56708
J1632–4818	16:32:39.70(3)	−48:18:53.8(8)	55426	1.228 996 4712(14)	−98.0730(3)	113	10.4	54220–58012
J1637–4553	16:37:58.692(4)	−45:53:26.82(9)	55443	8.419 397 382 52(19)	−22.6194(4)	159	11.1	53971–58012
J1637–4642	16:37:13.75(17)	−46:42:14.2(4)	55398	6.491 542 203(4)	−249.892(10)	128	10.4	54220–58012
J1638–4417	16:38:46.226(8)	−44:17:03.2(2)	55410	8.488 819 7965(4)	−11.5716(7)	128	10.4	54220–58012
J1638–4608	16:38:23.26(9)	−46:08:13.4(3)	55408	3.595 120 8300(10)	−66.5397(16)	129	10.4	54220–58012
J1640–4715	16:40:13.09(3)	−47:15:38.1(8)	55392	1.932 628 4729(4)	−15.7266(6)	128	10.4	54220–58012
J1643–4505	16:43:36.91(3)	−45:05:45.8(7)	55580	4.212 470 392(4)	−56.473(10)	116	9.6	54505–58012
J1648–4611	$16{:}48{:}22.043(7)$	$-46{:}11{:}15.75^{0.19}_{0.2}$	55395	6.062 160 6076(2)	−87.220(5)	125	10.4	54220–58012
J1649–4653	16:49:24.61(11)	−46:53:09.3(2)	55360	1.795 215 472 56(18)	−15.981 43(2)	125	10.4	54220–58012
J1650–4921	16:50:35.109(17)	−49:21:03.76(3)	55599	6.393 872 581 394(2)	−7.43411(5)	112	9.5	54548–58012
J1702–4306	17:02:27.36(2)	−43:06:45.1(4)	55560	4.640 188 780 13(2)	−21.057 20(2)	102	9.6	54505–58012
J1715–3903	$17{:}15{:}14.08(4)$	$-39{:}02{:}57.13^{0.06}_{0.12}$	55370	3.590 742 3095(9)	−48.2784(13)	128	10.4	54220–58012
J1722–3712	$17{:}22{:}59.21(4)$	$-37{:}12{:}04.51^{0.06}_{0.09}$	55362	4.234 063 3683(7)	−19.4742(11)	131	10.4	54220–58012
J1723–3659	17:23:07.58(17)	−36:59:14.2(8)	55384	4.932 793 178 87(3)	−19.5353(5)	128	10.4	54220–58012
J1733–3716	17:33:26.760(2)	−37:16:55.19(10)	55359	2.962 130 037 17(4)	−13.199 89(9)	129	11.1	53971–58012
J1735–3258	$17{:}35{:}56.66^{0.61}_{0.09}$	$-32{:}58{:}21.78^{0.46}_{0.38}$	55355	2.849 232 318 13(2)	−21.1107(3)	89	6.7	54220–56672
J1738–2955	$17{:}38{:}52.12(2)$	$-29{:}55{:}57.39^{0.22}_{0.15}$	55377	2.255 171 3364(2)	−41.7146(12)	89	6.8	54220–56709
J1739–2903	17:39:34.292(2)	−29:03:02.2(2)	55385	3.097 063 736 18(5)	−7.553 45(7)	135	10.4	54220–58012
J1739–3023	$17{:}39{:}39.79(4)$	$-30{:}23{:}12.87^{0.18}_{0.08}$	55351	8.743 419 4934(13)	−87.1129(2)	133	10.4	54220–58012
J1745–3040	17:45:56.316(12)	−30:40:22.9(11)	55276	2.721 579 246 363(8)	−7.904 60(4)	219	13.6	53035–58012
J1801–2154	$18{:}01{:}08.38^{0.63}_{0.05}$	$-21{:}54{:}07.51^{0.09}_{0.81}$	55385	2.664 522 569 01(11)	−11.3721(15)	84	6.8	54220–56708
J1806–2125	$18{:}06{:}19.59^{0.48}_{0.06}$	$-21{:}27{:}55.33^{0.98}_{0.48}$	55349	2.075 444 041(15)	−50.821(2)	123	11.0	53968–57992

Table 1 – *continued*

PSR	RAJ (h:m:s)	Dec.J (d:m:s)	PEPOCH	ν (s^{-1})	$\dot{\nu}$ ($10^{-14}\,s^{-2}$)	N_{ToA}	Time span (yr)	MJD range
J1809–1917	18:09:43.136(2)	−19:17:38.1(5)	55366	12.083 822 6201(8)	−372.7882(19)	130	10.4	54220–58012
J1815–1738	18:15:14.67(19)	$-17:38:06.95^{0.32}_{0.57}$	55364	5.038 875 458 88(10)	−197.4552(11)	86	6.8	54220–56708
J1820–1529	$18:20:41.11^{0.47}_{0.07}$	$-15:29:42.37^{0.08}_{0.29}$	55373	3.000 716 562(16)	−34.130(4)	81	7.4	53968–56671
J1824–1945	18:24:00.56(18)	$-19:46:03.47^{0.21}_{0.43}$	55291	5.281 57 555 2287(3)	−14.6048(5)	149	10.4	54220–58012
J1825–1446	18:25:02.96(17)	$-14:46:53.75^{0.72}_{0.68}$	55314	3.581 683 5827(4)	−29.0816(6)	132	10.4	54220–58012
J1828–1057	18:28:33.24(10)	−10:57:26.9(7)	55334	4.059 541 174 19(6)	−34.1114(4)	89	6.8	54220–56708
J1828–1101	18:28:18.8(13)	$-11:01:51.28^{0.02}_{0.93}$	55356	13.877 993 641(13)	−284.992(2)	131	11.1	53951–58012
J1830–1059	$18:30:47.51^{0.11}_{0.1}$	$-10:59:26.45^{0.88}_{0.74}$	55372	2.468 690 0068(5)	−36.5201(10)	154	10.4	54220–58012
J1832–0827	18:32:37.013(2)	−08:27:03.7(12)	55397	1.544 817 633 127(2)	−15.248 58(4)	124	10.4	54220–58012
J1833–0827	18:33:40.268(3)	−08:27:31.6(18)	55402	11.724 958 0817(4)	−126.1600(8)	124	10.2	54268–58012
J1834–0731	18:34:15.97(2)	−07:31:05.93(7)	55376	1.949 335 711 14(6)	−22.1210(7)	85	6.7	54268–56708
J1835–0944	18:35:46.653(6)	−09:44:27.2(4)	55130	6.880 068 960 72(4)	−20.7560(11)	41	3.7	54478–55822
J1835–1106	18:35:18.41(5)	−11:06:16.1(9)	55429	6.027 086 8794(10)	−74.7918(16)	125	10.2	54268–58012
J1837–0559	18:37:23.652(6)	−05:59:28.6(2)	55470	4.973 547 630 55(2)	−8.1858(4)	115	10.2	54303–58012
J1838–0453	18:38:11.4(12)	$-04:53:25.57^{0.32}_{0.83}$	55339	2.625 598 0205(5)	−80.1949(3)	91	6.6	54306–56708
J1838–0549	18:38:38.065(6)	−05:49:12.1(3)	55473	4.249 688 210 732(2)	−60.3601(5)	81	6.6	54306–56708
J1839–0321	18:39:37.520(8)	−03:21:10.8(3)	55522	4.187 917 144 798(2)	−21.9566(7)	70	6.6	54306–56708
J1839–0905	18:39:53.46(3)	−9:05:14.1(8)	54979	2.386 777 802 94(7)	−14.8244(10)	55	4.3	54268–55822
J1842–0905	18:42:22.15(2)	−09:05:30.0(3)	55392	2.901 527 844 74(2)	−8.8183(4)	126	10.2	54268–58012
J1843–0355	18:43:06.663(8)	−03:55:56.6(3)	55402	7.557 780 825 655(2)	−5.940 13(9)	84	7.5	53968–56708
J1843–0702	18:43:22.439(2)	−07:02:54.6(14)	55380	5.218 809 610 58(15)	−5.818 12(2)	128	10.2	54268–58012
J1844–0538	18:44:05.12(2)	−05:38:34.1(14)	55410	3.910 768 991 55(11)	−14.843 90(17)	122	10.2	54268–58012
J1845–0743	18:45:57.1833(4)	−07:43:38.57(2)	55336	9.551 586 249 996(12)	−3.345 425(2)	130	10.3	54267–58012
J1853–0004	18:53:23.027(8)	−00:04:33.4(3)	55446	9.858 325 73140(2)	−54.1604(5)	118	10.1	54306–58012
J1853 + 0011	18:53:29.980(8)	00:11:30.6(3)	55163	2.513 260 850 307(15)	−21.178 46(12)	37	3.4	54597–55822

Table 2. Prior ranges for the various stochastic and deterministic parameters used in the timing models. Δ_{param} is the uncertainty on a *parameter* from the initial TEMPO2 fitting.

Parameter	Prior range	Type
Red noise amplitude (A_{red})	(−20, −5)	Log-uniform
Red noise slope (β)	(0,20)	Log-uniform
EFAC	(−1,1.2)	Log-uniform
EQUAD	(−10, −3)	Log-uniform
Corner frequency (f_c)	($0.01/T_{span}$,$10/T_{span}$)	Log-uniform
Low frequency cut-off (LFC)	(−1,0)	Log-uniform
Sinusoid amplitude	(−10,0)	Log-uniform
Sinusoid phase	(0,2π)	Uniform
Log-sinusoid frequency	($1/T_{span}$, $100/T_{span}$)	Log-uniform
Proper motion	$\pm$ 1000 mas yr^{-1}	Uniform
RAJ, Dec.J, ν, $\dot{\nu}$, $\ddot{\nu}$	$\pm$ 10000 × Δ_{param}	Uniform

to Lentati & Shannon (2015), who state that a Bayes factor of >3 is strong and >5 is very strong. If multiple models have a Bayes factor greater than 5, we select model A, with a Bayes factor of X, if A is the simpler model and other models have Bayes factors not greater than $X + n$, where $n = 5$ is the threshold. All of these models are computed using the 'Bayesian young pulsar timing' pipeline that is cluster aware and simultaneously processes multiple models for each pulsar. We use ∼25 different timing models for each pulsar, leading to a total of 2125 models, which were processed in less than 15 h. The pipeline and the relevant instructions can be found in https://bitbucket.org/aparthas/youngpulsartiming.

The Bayesian pulsar timing approach is powerful because it allows for the simultaneous modelling of stochastic and deterministic parameters while also allowing for robust model selection based on the principles of Bayesian inference. The unique timing models that we use for each pulsar are:

(i) No stochastic parameters (NoSP),
(ii) Stochastic parameters using a power-law model (PL),
(iii) Stochastic parameters using a cut-off power-law model (CPL),
(iv) Proper motion and stochastic parameters (PL + PM),
(v) $\ddot{\nu}$ and stochastic parameters (PL + F2),
(vi) Model with low-frequency components and stochastic parameters (PL + LFC),
(vii) Model with a single sinusoidal fit and stochastic parameters (PL + SIN).

We choose wide prior ranges for the red noise amplitude and spectral index because timing noise in young pulsars is strong and can have a relatively steep spectral index. To perform an unbiased search for the proper motion, our prior distributions range from −1000 to +1000 mas yr^{-1}. Similarly, to ensure unbiased priors for position, spin, and spin-down parameters, the uncertainties of the initial least-squares fit values for each of these parameters are multiplied by 10^4.

Using various reasonable permutations of these models, we build more sophisticated timing models leading to a total of 25 different models per pulsar. It must be noted that in all of the above models, including the *NoSP* model, the position (RAJ and Dec.J) and the spin parameters (ν and $\dot{\nu}$) are fitted simultaneously with the other relevant model parameters.

Table 3. A summary of the preferred timing model, its Bayes factor compared to the base model, and 95 per cent confidence limits on the timing noise parameters ($A_{\rm red}$ and β) for each pulsar are reported. The first 19 pulsars listed have a significant detection of $\ddot{\nu}$ and n while for the rest the lower 2.5 perc ent and upper 97.5 perc ent confidence limits are reported from the PL + F2 model.

PSR	Best model	Bayes factor	$\log_{10}(A_{\rm red})$ ($\rm yr^{3/2}$)	β	$\ddot{\nu}$ ($10^{-23}\,\rm s^{-3}$)	n
J0857–4424	PL + F2	171.61	$-11.3^{+1.2}_{-0.6}$	$-9.1^{+3.8}_{-1.6}$	3.63(16)	2890(30)
J0954–5430	PL + F2	5.96	$-10.4^{+0.6}_{-0.3}$	$-4.4^{+2.1}_{-0.8}$	0.032(8)	18(9)
J1412–6145	PL + F2	29.99	$-10.7^{+1.1}_{-0.6}$	$-7.9^{+3.6}_{-1.6}$	0.62(4)	20(3)
J1509–5850	PL + F2	6.54	$-11.1^{+3.1}_{-2.1}$	$-5.1^{+8.6}_{-2.9}$	0.12(16)	11(3)
J1513–5908	PL + F2	44.08	$-9.7^{+0.4}_{-0.2}$	$-5.7^{+1.3}_{-0.6}$	189.6(2)	2.82(6)
J1524–5706	PL + F2	13.99	$-10.2^{+1.0}_{-0.7}$	$-3.6^{+3.6}_{-1.3}$	0.038(2)	4.2(7)
J1531–5610	PL + F2	100.57	$-11.8^{+1.3}_{-0.6}$	$-8.5^{+3.4}_{-1.6}$	1.37(2)	43(1)
J1632–4818	PL + F2	18.69	$-9.6^{+0.8}_{-0.5}$	$-5.0^{+2.7}_{-1.1}$	0.48(4)	6(1)
J1637–4642	PL + F2	54.34	$-9.7^{+0.6}_{-0.3}$	$-4.9^{+2.2}_{-0.9}$	3.2(15)	34(3)
J1643–4505	PL + F2 + LFC	3.24	$-10.1^{+0.5}_{-0.3}$	$-2.3^{+1.0}_{-0.4}$	0.11(2)	15(6)
J1648–4611	PL + F2	13.13	$-10.4^{+0.8}_{-0.5}$	$-6.3^{+2.3}_{-0.9}$	0.44(8)	40(10)
J1715–3903	PL + F2	4.19	$-9.2^{+0.2}_{-0.1}$	$-3.8^{+1.3}_{-0.6}$	0.4(11)	70(40)
J1738–2955	PL + F2	5.37	$-9.6^{+0.5}_{-0.2}$	$-5.8^{+2.4}_{-1.0}$	−0.5(16)	−70(40)
J1806–2125	PL + F2	5.56	$-9.1^{+0.3}_{-0.1}$	$-6.6^{+1.6}_{-0.7}$	1.1(4)	90(60)
J1809–1917	PL + PM + F2	94.14	$-11.7^{+1.1}_{-0.6}$	$-9.0^{+3.5}_{-1.4}$	2.70(3)	23.5(6)
J1815–1738	PL + F2 + LFC	3.18	$-11.8^{+3.1}_{-1.5}$	$-4.5^{+3.1}_{-1.4}$	0.73(8)	9(3)
J1824–1945	PL + F2 + LFC	32.02	$-10.9^{+0.3}_{-0.1}$	$-3.4^{+0.6}_{-0.3}$	0.05(2)	120(20)
J1830–1059	CPL + F2	19.55	$-8.5^{+0.3}_{-0.1}$	$-13.6^{+6.2}_{-2.8}$	0.16(19)	31(7)
J1833–0827	PL + F2	15.98	$-10.2^{+0.2}_{-0.1}$	$-2.8^{+1.2}_{-0.6}$	−0.19(13)	−15(2)
J0543 + 2329	PL	–	$-10.5^{+0.4}_{-0.2}$	$-3.6^{+1.8}_{-0.7}$	(−0.07,0.01)	(−2,10)
J0745–5353	PL + PM	20.13	$-10.5^{+0.5}_{-0.3}$	$-3.9^{+1.7}_{-0.6}$	(−0.01,0.02)	(−140,680)
J0820–3826	PL + LFC	6.15	$-11.1^{+1.8}_{-1.0}$	$-3.0^{+1.9}_{-0.8}$	(−0.15,0.06)	(−480,600)
J0834–4159	PL	–	$-10.9^{+1.2}_{-0.8}$	$-5.3^{+4.0}_{-1.5}$	(−0.02,0.02)	(−20,40)
J0905–5127	PL	–	$-9.6^{+0.2}_{-0.1}$	$-5.0^{+0.8}_{-0.4}$	(−0.06,0.14)	(−40,160)
J1016–5819	PL	–	$-11.5^{+1.6}_{-1.0}$	$-5.2^{+4.7}_{-1.8}$	(−0.04,0.01)	(−70,260)
J1020–6026	PL	–	$-11.9^{+4.2}_{-2.4}$	$-7.7^{+10.7}_{-4.7}$	(0.01,0.04)	(10,30)
J1043–6116	PL	–	$-10.7^{+0.5}_{-0.3}$	$-5.7^{+1.8}_{-0.7}$	(0.01,0.03)	(10,90)
J1115–6052	PL	–	$-10.5^{+0.7}_{-0.4}$	$-5.2^{+2.3}_{-0.9}$	(0.02,0.03)	(10,170)
J1123–6259	PL	–	$-10.1^{+0.3}_{-0.2}$	$-6.3^{+1.8}_{-0.8}$	(−0.05,0.1)	(−340,1300)
J1156–5707	PL	–	$-9.1^{+0.2}_{-0.1}$	$-5.6^{+0.9}_{-0.4}$	(−0.73, −0.04)	(−250,100)
J1216–6223	PL	–	$-11.0^{+1.6}_{-0.9}$	$-5.0^{+4.8}_{-2.3}$	(−0.01,0.01)	(−30,40)
J1224–6407	PL + LFC	11.09	$-11.6^{+0.5}_{-0.3}$	$-2.9^{+0.8}_{-0.4}$	(−0.05, −0.02)	(−200,100)
J1305–6203	PL	–	$-11.0^{+2.0}_{-1.3}$	$-6.1^{+5.9}_{-2.2}$	(0.01,0.02)	(1,20)
J1349–6130	PL	–	$-9.8^{+0.2}_{-0.1}$	$-4.7^{+1.0}_{-0.5}$	(−0.03,0.09)	(−200,1000)
J1452–5851	PL	–	$-11.4^{+2.4}_{-1.4}$	$-7.8^{+7.6}_{-2.9}$	(0.02,0.03)	(5,10)
J1453–6413	PL	–	$-10.3^{+0.2}_{-0.1}$	$-3.7^{+1.0}_{-0.4}$	(−0.01,0.02)	(−70,250)
J1512–5759	CPL	2.99	$-10.0^{+0.2}_{-0.1}$	$-7.0^{+2.5}_{-1.1}$	(−0.03,0.18)	(−10,130)
J1514–5925	PL	–	$-9.6^{+0.3}_{-0.1}$	$-3.6^{+1.6}_{-0.8}$	(−0.07,0.26)	(−300,1600)
J1515–5720	PL	–	$-9.8^{+0.2}_{-0.1}$	$-4.4^{+1.5}_{-0.6}$	(−0.02,0.08)	(−140,760)
J1530–5327	PL	–	$-10.8^{+0.7}_{-0.4}$	$-4.8^{+2.7}_{-1.1}$	(−0.02, −0.01)	(−200,70)
J1538–5551	PL	–	$-10.8^{+1.5}_{-1.0}$	$-5.1^{+4.8}_{-1.9}$	(−0.12,0.02)	(−140,100)
J1539–5626	PL	–	$-9.7^{+0.2}_{-0.1}$	$-5.1^{+1.0}_{-0.5}$	(−0.09,0.1)	(−570,1140)
J1543–5459	PL	–	$-9.2^{+0.2}_{-0.1}$	$-4.9^{+1.0}_{-0.5}$	(−0.2,0.21)	(−40,80)
J1548–5607	PL	–	$-10.1^{+0.3}_{-0.1}$	$-5.2^{+1.5}_{-0.6}$	(−0.06,0.08)	(−30,60)
J1549–4848	PL	–	$-9.7^{+0.2}_{-0.1}$	$-5.2^{+1.3}_{-0.6}$	(0.02,0.19)	(30,330)
J1551–5310	PL	–	$-9.1^{+0.4}_{-0.2}$	$-7.3^{+2.3}_{-1.0}$	(0.42,1.43)	(10,50)
J1600–5751	PL	–	$-10.0^{+0.2}_{-0.1}$	$-4.4^{+1.4}_{-0.6}$	(−0.06,0.04)	(−1000,1600)
J1601–5335	PL	–	$-9.6^{+0.5}_{-0.2}$	$-6.0^{+2.8}_{-1.2}$	(−0.21,0.32)	(−10,40)
J1611–5209	PL	–	$-10.1^{+0.2}_{-0.1}$	$-5.5^{+1.2}_{-0.5}$	(−0.09,0.03)	(−200,200)

Table 3 – *continued*

PSR	Best model	Bayes factor	$\log_{10}(A_{\rm red})$ ($\rm yr^{3/2}$)	β	$\ddot{\nu}$ ($10^{-23}\ \rm s^{-3}$)	n
J1632–4757	PL	–	$-10.6^{+1.3}_{-0.8}$	$-7.4^{+4.9}_{-1.9}$	(−0.04,0.17)	(−20,150)
J1637–4553	PL	–	$-10.3^{+0.3}_{-0.1}$	$-5.2^{+1.1}_{-0.5}$	(0.03,0.13)	(40,300)
J1638–4417	PL	–	$-10.0^{+0.4}_{-0.3}$	$-4.3^{+2.3}_{-0.9}$	(−0.07,0.08)	(−430,1000)
J1638–4608	PL	–	$-8.9^{+0.2}_{-0.1}$	$-4.0^{+1.2}_{-0.5}$	(−0.36,0.23)	(−30,40)
J1640–4715	PL	–	$-9.3^{+0.3}_{-0.1}$	$-5.3^{+1.6}_{-0.7}$	(0.06,0.31)	(45,330)
J1649–4653	PL	–	$-10.2^{+0.8}_{-0.4}$	$-8.0^{+3.3}_{-1.5}$	(−0.1,0.02)	(−75,60)
J1650–4921	PL	–	$-12.5^{+3.0}_{-1.8}$	$-7.4^{+7.8}_{-2.9}$	(0.01,0.02)	(25,100)
J1702–4306	PL + SIN	7.1	$-9.6^{+0.2}_{-0.1}$	$-3.5^{+0.8}_{-0.3}$	(−0.05,0.24)	(−50,360)
J1722–3712	PL	–	$-9.2^{+0.2}_{-0.1}$	$-4.2^{+0.8}_{-0.4}$	(−0.28,0.07)	(−320,270)
J1723–3659	PL	–	$-9.6^{+0.2}_{-0.1}$	$-5.9^{+1.4}_{-0.6}$	(−0.27,0.13)	(−340,420)
J1733–3716	PL	–	$-10.8^{+0.8}_{-0.4}$	$-5.6^{+2.5}_{-1.0}$	(−0.01,0.01)	(−20,35)
J1735–3258	PL	–	$-9.0^{+0.4}_{-0.2}$	$-4.6^{+2.1}_{-0.9}$	(−0.85,0.22)	(−540,510)
J1739–2903	PL	–	$-10.5^{+0.3}_{-0.2}$	$-4.1^{+1.6}_{-0.7}$	(0.01,0.02)	(3,85)
J1739–3023	PL	–	$-9.2^{+0.2}_{-0.1}$	$-3.1^{+0.8}_{-0.4}$	(−0.13,0.18)	(−15,40)
J1745–3040	PL	–	$-11.0^{+1.0}_{-0.6}$	$-5.3^{+2.3}_{-0.9}$	(−0.01,0.02)	(−20,30)
J1801–2154	PL	–	$-9.2^{+0.3}_{-0.1}$	$-3.6^{+1.4}_{-0.6}$	(−0.15,0.16)	(−305,720)
J1820–1529	PL + LFC	3.18	$-12.5^{+4.6}_{-1.9}$	$-6.9^{+3.8}_{-1.9}$	(−1.26,0.32)	(−320,290)
J1825–1446	PL	–	$-9.5^{+0.3}_{-0.2}$	$-3.9^{+1.2}_{-0.4}$	(−0.09,0.07)	(−40,70)
J1828–1057	PL	–	$-10.8^{+2.5}_{-1.6}$	$-5.6^{+6.6}_{-2.6}$	(0.01,0.03)	(4,15)
J1828–1101	PL	–	$-8.6^{+0.2}_{-0.1}$	$-3.7^{+0.8}_{-0.4}$	(−0.02,2.52)	(−1,60)
J1832–0827	PL	–	$-10.4^{+0.3}_{-0.1}$	$-5.1^{+1.4}_{-0.6}$	(−0.01,0.01)	(−10,10)
J1834–0731	PL	–	$-9.7^{+0.9}_{-0.6}$	$-4.1^{+3.7}_{-1.4}$	(−0.07,0.05)	(−30,50)
J1835–0944	PL	–	$-10.3^{+1.0}_{-0.6}$	$-5.2^{+6.9}_{-2.5}$	(−0.1,0.22)	(−150,640)
J1835–1106	PL	–	$-9.0^{+0.2}_{-0.1}$	$-4.4^{+0.9}_{-0.4}$	(−0.48,0.6)	(−50,120)
J1837–0559	PL	–	$-10.2^{+0.8}_{-0.5}$	$-4.9^{+3.0}_{-1.1}$	(−0.04,0.04)	(−300,620)
J1838–0453	PL	–	$-8.7^{+0.3}_{-0.1}$	$-5.7^{+1.4}_{-0.6}$	(−2.57, −0.37)	(−100,30)
J1838–0549	PL	–	$-10.8^{+1.6}_{-1.0}$	$-7.1^{+6.1}_{-2.2}$	(0.08,0.11)	(10,15)
J1839–0321	PL	–	$-10.1^{+2.1}_{-1.8}$	$-5.2^{+5.7}_{-1.1}$	(0.02,0.17)	(20,200)
J1839–0905	PL	–	$-9.4^{+0.4}_{-0.2}$	$-4.7^{+2.2}_{-0.9}$	(0.19,0.37)	(210,510)
J1842–0905	PL	–	$-9.4^{+0.2}_{-0.1}$	$-4.3^{+1.4}_{-0.6}$	(−0.1,0.09)	(−400,670)
J1843–0355	NoSP	2.64	NA	NA	NA	NA
J1843–0702	PL	–	$-10.4^{+0.5}_{-0.3}$	$-5.3^{+2.0}_{-0.8}$	(0.02,0.06)	(40,1350)
J1844–0538	PL	–	$-10.4^{+0.5}_{-0.2}$	$-5.7^{+2.2}_{-1.0}$	(−0.01,0.05)	(−6,150)
J1845–0743	PL	–	$-11.2^{+0.3}_{-0.2}$	$-2.2^{+1.4}_{-0.7}$	(−0.01,0.03)	(−60,85)
J1853–0004	PL	–	$-9.8^{+0.2}_{-0.1}$	$-6.3^{+1.3}_{-0.6}$	(−0.04,0.43)	(−10,230)

Table 4. Proper motions for two pulsars reported with their pulsar distance (as estimated from the DM in Yao et al. 2017) and the computed transverse velocities using the proper motion in right ascension ($V_{\alpha \rm T}$) and total ($V_{\rm T}$). The error bars reported are 95 per cent confidence limits. The epoch for the position is the same as the epoch of the period reported in Table 1.

PSR	μ_α	μ_δ	$\mu_{\rm tot}$	Distance	$V_{\alpha \rm T}$	$V_{\rm T}$
	($\rm mas\ yr^{-1}$)	($\rm mas\ yr^{-1}$)	($\rm mas\ yr^{-1}$)	(kpc)	($\rm km\ s^{-1}$)	($\rm km\ s^{-1}$)
J0745–5353	−60(10)	50(10)	80(10)	0.57	–	220(30)
J1809–1917	−19(6)	50(90)	60(90)	3.27	−300(100)	900(1300)

4 RESULTS

In Table 1, we present the position and spin parameters for the pulsars in our sample with their 95 per cent credible regions as calculated from the posterior distributions along with their observation timespan. Table 2 provides a list of unique parameters used in our different timing models along with their prior ranges. Fig. 2 shows the timing residuals from the preferred model, without subtracting the modelled timing noise.

This is the first time that the timing noise has been consistently modelled using Bayesian inference for a large sample of young pulsars. In Table 3, we present the preferred timing model, the Bayes factor of that model relative to the base model, which in this case is the model in which the position, spin frequency, spin frequency derivative, and a power-law timing noise are fitted for.

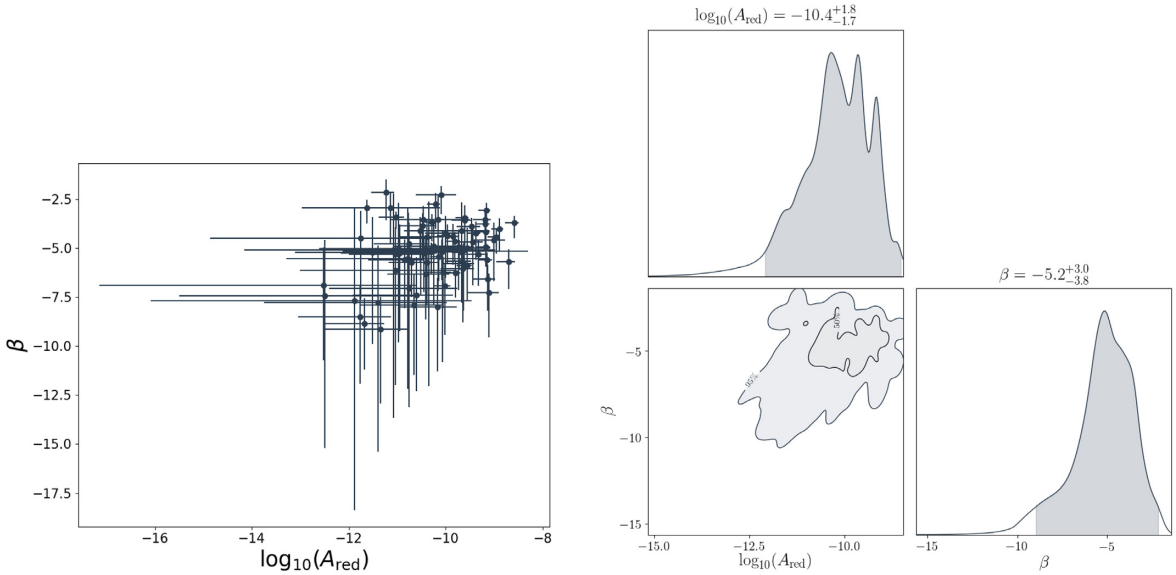

Figure 3. *Left:* The distribution of red noise amplitude against spectral indices for our sample of pulsars for which a power-law timing model is preferred. The error bars are 95 per cent confidence limits obtained from the preferred model. *Right:* Posterior distribution of the red noise amplitude and spectral indices from the preferred model for each pulsar are normalized and added together to form an integrated posterior distribution as shown here.

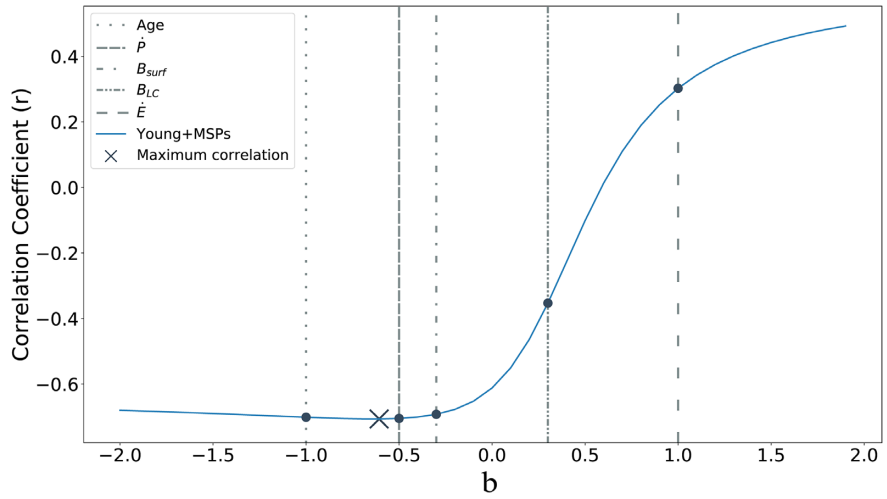

Figure 4. The relationship between the correlation coefficient (r), which measures the strength of the timing noise for various values of $\sigma_{\rm P}$ and b, for a fixed value of $a = 1$.

The Bayes factor is zero if the preferred model is the base model (PL). For the first 19 pulsars listed, we report significant detections of $\ddot{\nu}$ and the derived braking index values (n) from the preferred model, while for the rest, we report their upper and lower limits as derived from the PL + F2 model. The braking index is estimated by using equation (2) on the entire posterior distribution of ν, $\dot{\nu}$, and $\ddot{\nu}$. The values for $A_{\rm red}$ and β are derived from the preferred model as stated in the second column.

We find that for two pulsars, PSR J1843–0355 and PSR J1853+0011, a model without the timing noise is preferred, while for 58 other pulsars, a model with only the power-law timing noise is strongly preferred. There is marginal to strong evidence for the presence of low-frequency components which are much longer than the data set for 5 pulsars. We find marginal evidence supporting a cut-off frequency in the power-law timing noise model for PSR J1512–5759.

A model with a $\ddot{\nu}$ is preferred for 19 pulsars, out of which for 3 pulsars, the model with low-frequency components is preferred, and for one other pulsar a model with a proper motion is preferred. The braking indices for these pulsars, along with the implications on glitch recovery models and pulsar spin-down are discussed in a second paper (Parthasarathy et al., in preparation). A model with only the proper motion is preferred for PSR J0745–5353. Table 4 lists the values for the proper motion in right ascension and declination in mas yr^{-1}, i.e. $\mu_\alpha = \dot{\alpha}\cos\delta$ and $\mu_\delta = \dot{\delta}$ and contains the computed transverse velocity using the distance derived from the DM using the electron-density model of Yao, Manchester & Wang (2017). PSR J1702–4306 shows indication for periodic modulation in its ToAs, which is discussed further in Section 5.3. It was noted that for PSR J1830–1059, an unpublished glitch was reported,[2] on

[2]http://www.jb.man.ac.uk/pulsar/glitches/gTable.html

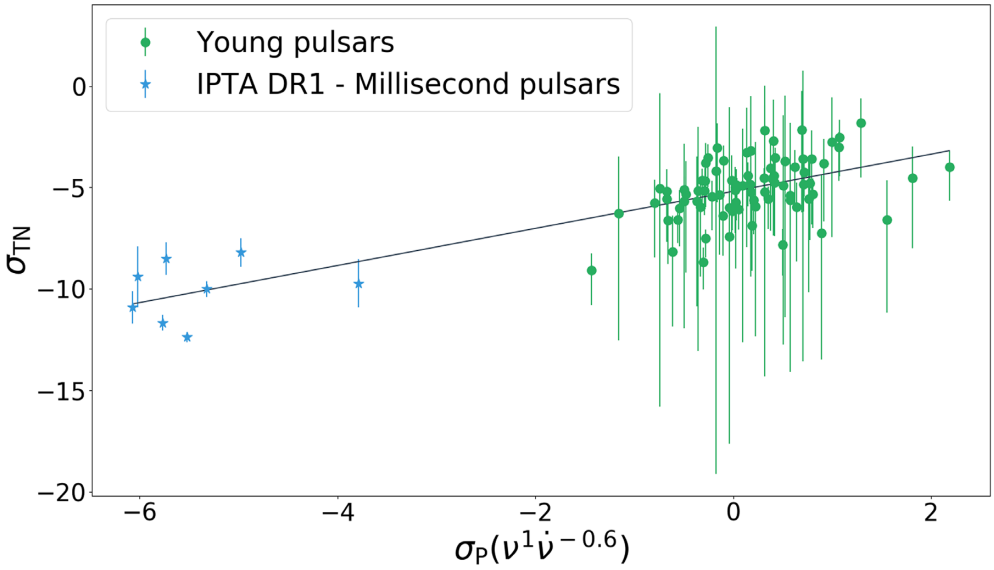

Figure 5. Relationship between the timing noise strength and the timing noise metric at the maximally correlated values of a and b for our sample of young pulsars and MSPs from the International Pulsar Timing Array data release 1 (IPTA DR1) sample.

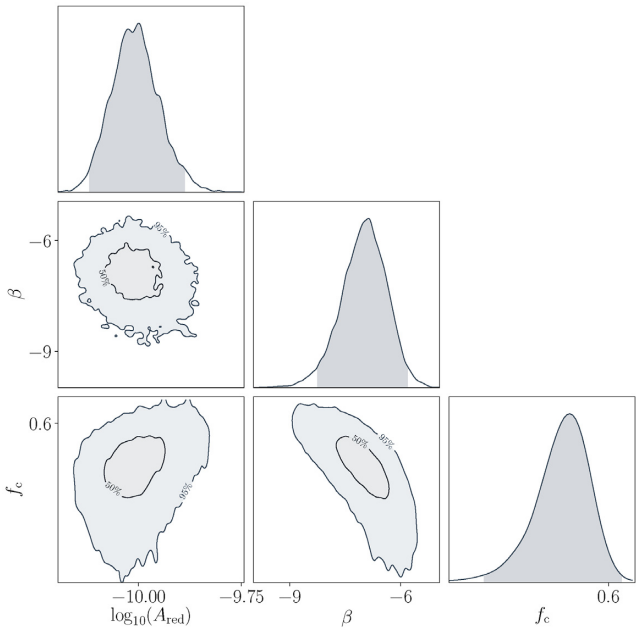

Figure 6. Posterior distribution of the corner frequency parameter along with the timing noise parameters for PSR J1512–5759. This model is positively preferred with a Bayes factor of 3.23.

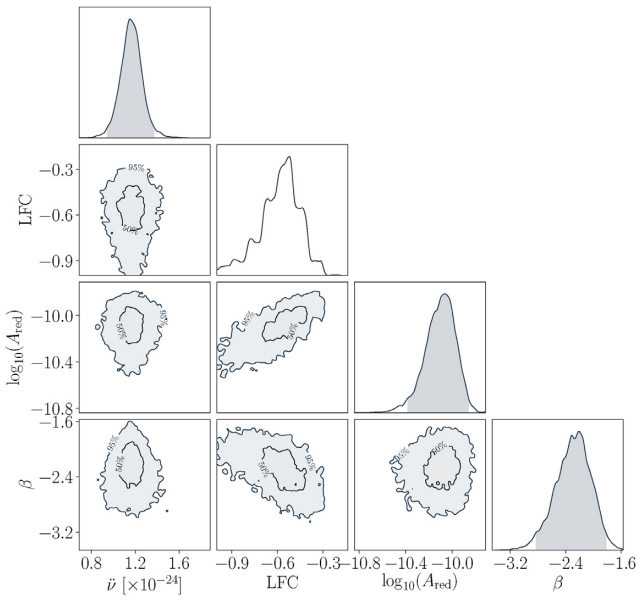

Figure 7. Posterior distribution of the low-frequency component, a $\ddot{\nu}$ along with the timing noise parameters for PSR J1643–4505.

2009 July 29 (MJD 55041). For this pulsar a model with a glitch, a $\ddot{\nu}$, and a cut-off power-law fit is preferred. It is interesting to note here that we find an evidence for a cut-off frequency for only two pulsars out of the 85 in our sample.

Fig. 3 shows the distribution of A_{red} and β extracted from the preferred model for each pulsar in our sample except for the two pulsars for which the cut-off power-law model is preferred. The errors shown in the plot are the 2.5 per cent and 97.5 per cent confidence limits on both the parameters. The median value for $\log_{10}(A_{red})$ is $-10.4^{+1.8}_{-1.7}$ yr$^{3/2}$ and for β is $-5.2^{+3.0}_{-3.8}$. Fig. 3 also shows the integrated posterior distribution for the timing noise parameters. Contours are plotted for the 50 per cent and 95 per cent confidence intervals with the accompanying histograms.

We test the robustness of the timing noise model by comparing them to an independent Bayesian analysis tool, ENTERPRISE[3] (Enhanced Numerical Toolbox Enabling a Robust Pulsar Inference Suite), which is developed for timing noise and gravitational wave analysis in pulsar timing data. With ENTERPRISE, we use a Parallel-Tempering Ensemble Markov Chain Monte Carlo (PTMCMC) sampler. The prior ranges for the noise models are identical and in both the cases the red noise is modelled as a power law. Since ENTERPRISE does not allow for full non-linear sampling of the timing

[3]https://github.com/nanograv/enterprise

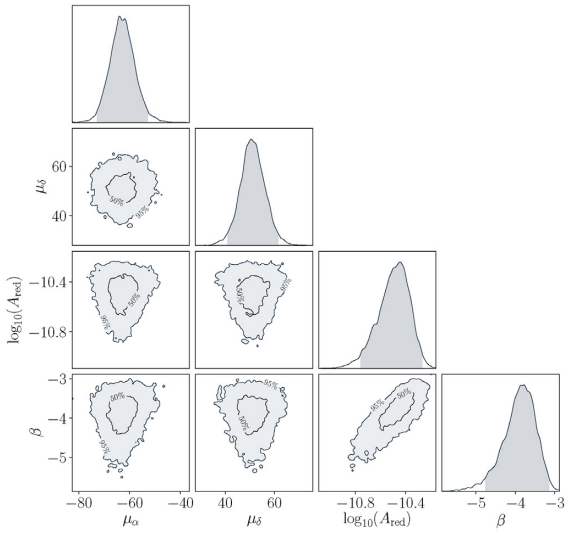

(a) Posterior distribution of the proper motion and the timing noise parameters for PSR J0745–5353.

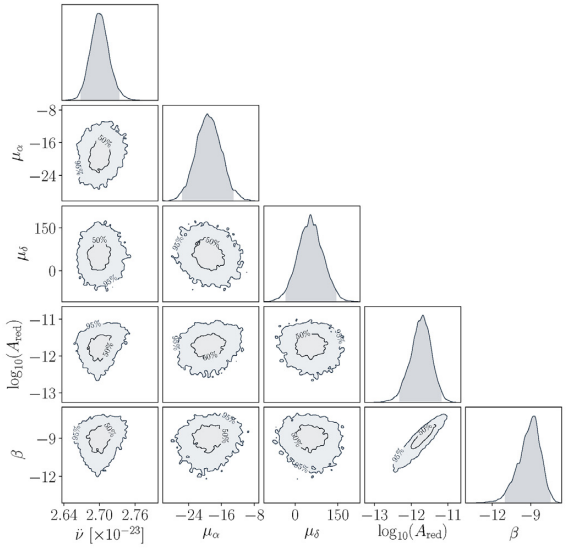

(b) Posterior distribution of the proper motion, $\ddot{\nu}$ and the timing noise parameters for PSR J1809–1917.

Figure 8. (a) Posterior distribution of the proper motion and the timing noise parameters for PSR J0745–5353. (b) Posterior distribution of the proper motion, $\ddot{\nu}$ and the timing noise parameters for PSR J1809–1917.

model and only does implicit marginalization over the parameters in the linear perturbation regime, we compare the noise models for the pulsars that prefer the power-law model only. The distributions are similar to that shown in Fig. 3 with median values of the $\log_{10}(A_{\rm red})$ and β being, $-10.4^{+1.8}_{-1.7}$, $-10.3^{+1.6}_{-1.8}$ and $-5.2^{+3.0}_{-3.8}$, -5.2 ± 3.3 using TEMPONEST and ENTERPRISE, respectively.

5 DISCUSSION

5.1 Timing noise

Various attempts have been made to quantify timing noise in pulsars. Cordes & Helfand (1980) proposed an 'activity parameter' (A) that measured the timing noise relative to the Crab pulsar,

$$A = \log_{10}\left[\frac{\sigma_{\rm TN,2}(T)}{\sigma_{\rm TN,2}(T)_{\rm Crab}}\right], \tag{12}$$

where $\sigma_{\rm TN,2}(T)$ is the rms residual phase from a second-order least-squares polynomial fit. They found that this parameter is strongly correlated with the characteristic age of the pulsars. Arzoumanian et al. (1994) measured the strength of the timing noise (Δ_8) after a cubic polynomial fit to the ToAs over a time period (T_8), of 10^8 s and found a strong correlation with the pulsar period derivative,

$$\Delta_8 = \log_{10}\left(\frac{|\ddot{\nu}|}{6\nu}T_8^3\right). \tag{13}$$

Shannon & Cordes (2010) argued that statistics based on a cubic fit ($\ddot{\nu}$) underestimates the strength of the timing noise and proposed that the rms timing noise after a second-order fit is a more accurate diagnostic [i.e. they simply use $\sigma_{\rm TN,2}(T)$ without the Crab as reference]. They also developed a metric ($\sigma_{\rm P}$),

$$\sigma_{\rm P} = C_2 \nu^{\alpha} |\dot{\nu}|^{\beta} T^{\gamma}, \tag{14}$$

which linked the timing noise with the measured pulsar parameters. Using a maximum likelihood approach they determined the coefficients α, β, γ, and the scaling factor ($C2$) given the pulsar parameters and the time span (T).

We characterize the strength of the timing noise in our pulsars using the equation,

$$\log_{10}({\sigma_{\rm TN}}^2) = 2\log_{10}(A_{\rm red}) + \log_{10}\left(\frac{T}{1{\rm yr}}\right)(\beta - 1), \tag{15}$$

where T signifies the time span over which $\ddot{\nu}$ is measured. Previous metrics for timing noise relied upon modelling it as either a second order or a cubic polynomial which directly affected the measurements of higher order spin-down parameters. Since we characterize the timing noise as a power law using the amplitude and spectral index, it allows us to measure an unbiased value for the pulsar spin-down parameters.

To determine the correlation between different pulsar parameters and the strength of the timing noise ($\sigma_{\rm TN}$), we perform a linear least-squares regression analysis between $\sigma_{\rm TN}$ (with $T = 10$ yr) and $\sigma_{\rm P}$,

$$\sigma_{\rm P} = \nu^{a} |\dot{\nu}|^{b}. \tag{16}$$

The correlation coefficient (r) is computed in a linear regression analysis. We search over the parameter space spanned by arbitrary scaling coefficients, a and b to find the maximally correlated scaling relationship.

The various pulsar parameters can then be expressed in terms of ν and $\dot{\nu}$ as

(i) Spin-period derivative: $\nu^{-2}|\dot{\nu}|^{1}$
(ii) Spin-down age: $\nu^{1}|\dot{\nu}|^{-1}$
(iii) Surface magnetic field strength: $\nu^{-3/2}|\dot{\nu}|^{1/2}$
(iv) Magnetic field at the light cylinder: $\nu^{3/2}|\dot{\nu}|^{1/2}$
(v) Rate of loss of rotational kinetic energy: $\nu^{1}|\dot{\nu}|^{1}$

and are represented in Fig. 4.

Since the correlation coefficients maintain rotational symmetry in the (a, b) plane and following the discussion in Jankowski et al. (2018), any combination of (a, b) that has the same ratio will have the same correlation coefficient. For example, the spin-down derivative can be expressed as $\nu^{1}|\dot{\nu}|^{-1/2}$ or $\nu^{-2}|\dot{\nu}|^{1}$. In our analysis, we set the $a = 1$, which results in the various pulsar parameters being expressed as a function of b as shown in Fig. 4. We then find that

the maximum absolute correlation coefficient for $\sigma_{\rm TN}$ occurs at $b = -0.9 \pm 0.2$ for our sample of young pulsars.

This suggests that the timing noise is more closely correlated with spin-period derivative and spin-down age of the pulsar as compared to $\dot{E}$. Analysing the relationship of the timing noise with observing time span, we find no evidence for band-limited timing noise, which would be expected to flatten over longer timing baselines. We compare our results with those of Shannon & Cordes (2010), who reported a scaling relation of $\nu^{-0.9\pm0.2}|\dot{\nu}|^{1.0\pm0.05}$, which can also be expressed as $\nu^{1}|\dot{\nu}|^{-1.1\pm0.2}$. We find that our scaling relationships are consistent with those reported by Shannon & Cordes (2010).

To test the robustness of this correlation, we also include the timing noise parameters of 8 MSPs from a sample of 49 pulsars from the International Pulsar Timing Array Data release 1 (Verbiest et al. 2016) for which the preferred stochastic model is the spin-noise process[4] (Lentati et al. 2016). The MSPs have a typical observing span of ∼10 yr and the timing noise is modelled as a power-law process using TEMPONEST. We find that on adding the MSPs to our sample, we obtain a stronger correlation and the maximum absolute correlation occurs for $b = -0.6 \pm 0.1$, (Fig. 4). van Haasteren & Levin (2013) derive an expression (equation 22 in their paper) for relating the power spectral density to the average rms in the post-fit timing residuals, which can be used to relate T^{γ} in equation (14) to β in equation (15) as $\gamma = \frac{\beta-1}{2}$. From such a relation, we obtain a value of γ to be 2 ± 0.1, consistent with Shannon & Cordes (2010). The correlation coefficients obtained for pulsar age, $\dot{E}$ and magnetic field strength are also shown in Fig. 4.

Fig. 5 shows the correlation between $\sigma_{\rm TN}$ and the timing noise metric ($\sigma_{\rm P}$) for $a = 1$ and $b = -0.6 \pm 0.1$. For the young pulsar sample, the error bars are 95 per cent confidence limits computed from the measured posterior distributions, while for the MSPs, they are adopted from the 1σ confidence limits from Lentati et al. (2016). It is evident that the timing noise is stronger in young pulsars as compared to older pulsars (MSPs) in which case, we measure smaller values for the red-noise amplitude and shallower spectral indices. Our parametrization of timing noise from measured values of $A_{\rm red}$ and β can be used to predict the relative strength of timing noise in new pulsars given their spin-down parameters.

We find marginal evidence for the presence of a corner frequency ($f_{\rm c}$) in PSR J1512–5759. The posterior distribution of the corner frequency and the timing noise parameters for this pulsar are shown in Fig. 6. We find that for five pulsars, a model with a low-frequency component (LFC) is preferred. This model implements extra sinusoidal fits at frequencies much longer than the data set. It is worth noting here that the measurement of low-frequency components is strongly correlated with the amplitude of the red noise (see Fig. 7) in the timing residuals. The prospects of detecting signatures at low frequencies are greater when the red-noise amplitude is larger. This is clearly reflected in the Bayes factors obtained for both PSR J0820–3826 (BF of 6.15) and PSR J1820–1529 (BF of 3.18), which have measured red-noise amplitudes of $-11.1^{1.8}_{1.0}$ and $-12.5^{4.6}_{1.9}$ yr$^{3/2}$, respectively. For PSR J1643–4505, although the Bayes factor is just 3.24, the measured red-noise amplitude is relatively larger ($-10.1^{0.5}_{0.3}$ yr$^{3/2}$), thus leading to a relatively well-constrained posterior for the LFC parameter as shown in Fig. 7. The low Bayes factor can perhaps be attributed to the additional detection of $\ddot{\nu}$.

[4]Uncertainties in the Solar System Barycenter (SSB) have been identified to introduce rednoise signatures in the ToAs of the highest precision MSPs; however, those effects are sub-dominant in the MSP data sets studied here (Arzoumanian et al. 2018)

5.2 Proper motions and pulsar velocities

For the two pulsars listed in Table 4, the posterior distributions of the proper motions are shown in Fig. 8.

PSR J0745–5353 shows a clear detection of a proper motion signature. Assuming a distance of 0.57 kpc, the derived transverse velocity of 220 ± 30 km s^{-1} is typical of the population of pulsars as a whole. For PSR J1809–1917, we measure a significant proper motion in right ascension, while the proper motion in declination is consistent with zero. The transverse velocity computed from μ_{α} is ∼300 kms^{-1}, which is reasonable in terms of the transverse velocities for the general pulsar population.

PSR J1745–3040 has a previously reported proper motion from both the frequentist method (Zou et al. 2005), with μ_{α} of 6 ± 3 mas yr^{-1}, μ_{δ} of 4 ± 26 mas yr^{-1} and the Bayesian method (Li et al. 2016), with μ_{α} of 11.9 ± 16 mas yr^{-1}, μ_{δ} of 50 ± 12 mas yr^{-1}. In our analysis the proper motion model is marginally better than the power-law model (PL) with a Bayes factor of 2. From this model, we obtain a μ_{α} of 9.9 ± 3.5 mas yr^{-1} and a μ_{δ} of 10.5 ± 27.6, which are consistent with the previous measurements. PSR J1833–0827 has a previously reported timing proper motion (Hobbs et al. 2005), but the preferred model in our analysis shows a strong detection of $\ddot{\nu}$.

There are two other pulsars, PSR J1453–6413 (Bailes et al. 1990) and J1825–1446 (Dexter et al. 2017) that have a previously reported interferometric proper motions with greater than 3σ significance. In our analysis, the uncertainties associated with the proper motion measurements are quite large for these pulsars with the preferred models being a power-law model for PSR J1453–6413 and a sinusoidal fitting model for PSR J1825–1446.

Unbiased measurements of proper motion and other such deterministic parameters in pulsars that are strongly contaminated with timing noise strongly underscores the evidence-based model selection that we have employed here. Increasing the timing baselines will help to discover further significant proper motion measurements.

5.3 Pulsars with planetary companions?

To search for periodic modulations in our pulsars, we fit for a sinusoid with varied amplitudes, phases, and frequencies and compare the evidences to choose the preferred model. Here we comment on five pulsars present in our sample that have been previously studied in the context of periodic signals in their timing residuals.

PSR J1637–4642 was reported to show marginal evidence for a single sinusoid in Kerr et al. (2016). We find that the preferred model for this pulsar is PL + F2. In order to further test this, we fitted for a sinusoid simultaneously with $\ddot{\nu}$ but find that this model (PL + F2 + SIN) only has a Bayes Factor of 2.9, which does not pass a Bayes factor threshold of 5 over the much simpler model.

PSR J1825–1446 showed strong evidence for a single sinusoid according to Kerr et al. (2016). We however find that, the PL + SIN model does not meet the threshold to be preferred over the PL model. The model with a sinusoidal fitting has a Bayes factor of only 1.7.

For PSR J1830–1059, we find evidence for a glitch with parameters similar to those in the catalogue and find that the best model is one which includes the glitch, $\ddot{\nu}$ and a cut-off power-law model. This pulsar is notable for correlated profile and $\dot{\nu}$ changes (Brook et al. 2016; Kerr et al. 2016). Stairs et al. (2019) performed an exhaustive analysis on multihour long observations of this pulsar

and reported that the pulsar undergoes mode changing between two stable, extreme profile states. They stated that the observed mode transition rate can perhaps be explained by the chaotic behaviour model as previously suggested by Seymour & Lorimer (2013). The detection of a glitch in 2009, further complicates the theoretical models invoking explanations based on pinned vortices inside neutron stars. We conclude that the deviation from a simple power law, the presence of a glitch and the identified mode changing makes this pulsar more complex and demands further investigation.

PSR J1638–4608 was reported to show a strong evidence for a single sinusoid fitting in Kerr et al. (2016). Close examination however revealed the presence of two new glitches. The amplitudes of these are glitches are very small, of the order of 10^{-8} and 10^{-9} Hz. We find that, after taking the glitches into account, the glitch inclusive model (GL + SIN) has a Bayes factor of ∼60 as compared to the model with only the stochastic parameters (PL).

It is useful to note here that although the pulsars presented in this analysis were manually selected to not have any identified glitches in the data set, we subsequently found that the two pulsars discussed above had detected glitches. This was missed in the initial manual search owing to the small glitch amplitudes. We decided to retain them in the paper, because for one of the sources, the glitches were unpublished, while for the other, it significantly changed the favoured model.

For PSR J1702–4306, Kerr et al. (2016) saw strong evidence for a single sinusoid with a projected semimajor axis (a_n) of 2.9 ± 0.7 ms and an orbital period (P_b) of 391 ± 10 d. In our data, we find that the sinusoidal model is strongly preferred over the PL model by a Bayes factor of 7.1. We measure a_n to be 2.6 ± 0.2 ms and P_b to be 316 d. It is unclear if these effects are caused due to neutron star precession or due to the presence of a planetary companion, as discussed in Kerr et al. (2016).

6 CONCLUSIONS

We have applied an improved methodology based on Bayesian inference on a large sample of high $\dot{E}$, young pulsars to measure different stochastic and deterministic parameters of interest. We have shown that evidence-based model selection is a powerful technique to disentangle stochastic processes from deterministic ones and to obtain unbiased measurements of pulsar parameters. For each pulsar in our sample, a total of 25 different models were compared and the best model was selected based on a Bayes factor threshold of 5. The power-law model was preferred for 58 pulsars, while we found no evidence of timing noise in two pulsars. The low-frequency component (PL + LFC) model was preferred for 5 pulsars and in two other pulsars we measure a proper motion signature. Marginal evidence for the presence of a corner frequency in the power law was detected in two pulsars. We report two new glitches in PSR J1638–4608 and find evidence for periodic modulation in the ToAs of both PSR J1638–4608 and PSR J1702–4306. We have also compared our timing noise models with an independent Bayesian package, ENTERPRISE, and obtained consistent results.

We characterize the timing noise as a power law based on the red-noise amplitude (A_{red}) and spectral index (β) and report that there is a strong correlation between the spin-period derivative of the pulsar and the strength of the timing noise. We develop a metric that can be used to determine the relative strength of the timing noise in any pulsar given its spin-down parameters. On adding MSPs to our sample, we notice that the correlation gets stronger, which is consistent with what is expected.

Finally, we measure significant $\ddot{\nu}$ measurements for 19 pulsars and also report their braking indices. We discuss the significance of the braking index measurements, their robustness and the effects of glitch recovery models in a subsequent publication.

ACKNOWLEDGEMENTS

The Parkes radio telescope is part of the Australia Telescope, which is funded by the Commonwealth Government for operation as a National Facility managed by CSIRO. AP would like to thank Marcus Lower and Daniel Reardon for their comments and ideas. AP would also like to thank Andrew Jameson for the continued support in installing TEMPONEST on the OzSTAR High performance computing (HPC) facility. This work made use of the gSTAR and OzSTAR national HPC facilities. gSTAR is funded by Swinburne and the Australian Government Education Investment Fund. OzSTAR is funded by Swinburne and the National Collaborative Research Infrastructure Strategy (NCRIS). This work is supported through Australian Research Council (ARC) Centre of Excellence CE170100004. AP is grateful to CSIRO Astronomy and Space Science for support throughout this work. RMS acknowledges support through ARC grant CE170100004. MB acknowledges support through ARC grant FL150100148. Work at NRL is supported by NASA. This work also made use of standard PYTHON packages (Jones et al. 2001; Oliphant 2006; Hunter 2007; McKinney 2010), Chainconsumer (Hinton 2016), and Bokeh (Bokeh Development Team 2018).

REFERENCES

Abdo A. A. et al., 2013, ApJS, 208, 17
Alpar M. A., Nandkumar R., Pines D., 1985, ApJ, 288, 191
Anderson P. W., Itoh N., 1975, Nature, 256, 25
Arzoumanian Z., Nice D. J., Taylor J. H., Thorsett S. E., 1994, ApJ, 422, 671
Arzoumanian Z. et al., 2018, ApJS, 235, 37
Bailes M., Manchester R. N., Kesteven M. J., Norris R. P., Reynolds J. E., 1990, MNRAS, 247, 322
Bokeh Development Team, 2018, Bokeh: Python library for interactive visualization, https://bokeh.pydata.org/en/latest/
Boynton P. E., Groth E. J., Hutchinson D. P., Nanos G. P., Partridge R. B., Wilkinson D. T., 1972, ApJ, 175, 217
Brook P. R., Karastergiou A., Johnston S., Kerr M., Shannon R. M., Roberts S. J., 2016, MNRAS, 456, 1374
Caballero R. N. et al., 2016, MNRAS, 457, 4421
Cheng K. S., 1987a, ApJ, 321, 799
Cheng K. S., 1987b, ApJ, 321, 805
Coles W., Hobbs G., Champion D. J., Manchester R. N., Verbiest J. P. W., 2011, MNRAS, 418, 561
Cordes J. M., Greenstein G., 1981, ApJ, 245, 1060
Cordes J. M., Helfand D. J., 1980, ApJ, 239, 640
Cui X. H., Wang H. G., Xu R. X., Qiao G. J., 2007, A&A, 472, 1
Dexter J. et al., 2017, MNRAS, 471, 3563
Espinoza C. M., Lyne A. G., Stappers B. W., 2017, MNRAS, 466, 147
Feroz F., Hobson M. P., Bridges M., 2009, MNRAS, 398, 1601
Feroz F., Hobson M. P., Bridges M., 2011, Astrophysics Source Code Library, record ascl:1109.006
Greenstein G., 1970, Nature, 227, 791
Groth E. J., 1975, ApJS, 29, 453
Harrison E. R., Tademaru E., 1975, ApJ, 201, 447
Hinton S. R., 2016, J. Open Source Softw., 1, 00045
Hobbs G., Lyne A. G., Kramer M., Martin C. E., Jordan C., 2004, MNRAS, 353, 1311
Hobbs G., Lorimer D. R., Lyne A. G., Kramer M., 2005, MNRAS, 360, 974
Hobbs G. B., Edwards R. T., Manchester R. N., 2006, MNRAS, 369, 655

Hotan A. W., van Straten W., Manchester R. N., 2004, Publ. Astron. Soc. Aust., 21, 302
Hulse R. A., Taylor J. H., 1975, ApJ, 195, L51
Hunter J. D., 2007, Comput. Sci. Eng., 9, 90
Jankowski F., van Straten W., Keane E. F., Bailes M., Barr E. D., Johnston S., Kerr M., 2018, MNRAS, 473, 4436
Johnston S., Galloway D., 2000, in Kramer M., Wex N., Wielebinski R., eds, ASP Conf. Ser., Vol. 202, IAU Colloq. 177: Pulsar Astronomy – 2000 and Beyond. Astron. Soc. Pac., San Francisco, p. 599
Johnston S., Karastergiou A., 2017, MNRAS, 467, 3493
Johnston S., Hobbs G., Vigeland S., Kramer M., Weisberg J. M., Lyne A. G., 2005, MNRAS, 364, 1397
Jones P. B., 1990, MNRAS, 246, 364
Jones E. et al., 2001, SciPy: Open source scientific tools for Python
Kerr M., Johnston S., Hobbs G., Shannon R. M., 2015, ApJ, 809, L11
Kerr M., Hobbs G., Johnston S., Shannon R. M., 2016, MNRAS, 455, 1845
Kramer M., Lyne A. G., O'Brien J. T., Jordan C. A., Lorimer D. R., 2006, Science, 312, 549
Lai D., Goldreich P., 2000, ApJ, 535, 402
Lai D., Qian Y.-Z., 1998, ApJ, 505, 844
Lam M. T. et al., 2017, ApJ, 834, 35
Lentati L., Shannon R. M., 2015, MNRAS, 454, 1058
Lentati L., Alexander P., Hobson M. P., Taylor S., Gair J., Balan S. T., van Haasteren R., 2013, Phys. Rev. D, 87, 104021
Lentati L., Alexander P., Hobson M. P., Feroz F., van Haasteren R., Lee K. J., Shannon R. M., 2014, MNRAS, 437, 3004
Lentati L. et al., 2016, MNRAS, 458, 2161
Li L., Wang N., Yuan J. P., Wang J. B., Hobbs G., Lentati L., Manchester R. N., 2016, MNRAS, 460, 4011
Link B., 2012, MNRAS, 422, 1640
Link B., Epstein R. I., 2001, ApJ, 556, 392
Lyne A., Hobbs G., Kramer M., Stairs I., Stappers B., 2010, Science, 329, 408
Manchester R. N., 2004, Science, 304, 542
McKinney W., 2010, in Assoufid L., Takacs P. Z., Asundi A. S., eds, Proc. SPIE Conf. Ser., Vol. 7801, Advances in Metrology for X-Ray and EUV Optics III. SPIE, Bellingham, p. 780106
Melatos A., Link B., 2014, MNRAS, 437, 21
Melatos A., Peralta C., Wyithe J. S. B., 2008, ApJ, 672, 1103
Oliphant T., 2006, NumPy: A Guide to NumPy. Trelgol Publishing, USA
Petroff E., Keith M. J., Johnston S., van Straten W., Shannon R. M., 2013, MNRAS, 435, 1610
Reardon D. J. et al., 2016, MNRAS, 455, 1751
Ruderman M., 1969, Nature, 223, 597
Seymour A. D., Lorimer D. R., 2013, MNRAS, 428, 983
Shannon R. M., Cordes J. M., 2010, ApJ, 725, 1607
Shannon R. M., Johnston S., Manchester R. N., 2014, MNRAS, 437, 3255
Smith D. A. et al., 2008, A&A, 492, 923
Stairs I. H., Lyne A. G., Shemar S. L., 2000, Nature, 406, 484
Stairs I. H. et al., 2019, MNRAS, 3230, 485
Staveley-Smith L. et al., 1996, Publ. Astron. Soc. Aust., 13, 243
van Haasteren R., Levin Y., 2013, MNRAS, 428, 1147
Verbiest J. P. W. et al., 2016, MNRAS, 458, 1267
Weltevrede P. et al., 2010, Publ. Astron. Soc. Aust., 27, 64
Wolszczan A., Frail D. A., 1992, Nature, 355, 145
Yao J. M., Manchester R. N., Wang N., 2017, ApJ, 835, 29
Zou W. Z., Hobbs G., Wang N., Manchester R. N., Wu X. J., Wang H. X., 2005, MNRAS, 362, 1189

APPENDIX A: POSTERIOR DISTRIBUTIONS

The posterior distributions of the preferred model for six pulsars are shown in Fig. A1 as a sample. Please visit the online repository https://bitbucket.org/aparthas/youngpulsartiming to view the posterior distributions for all of the 85 pulsars discussed in this paper.

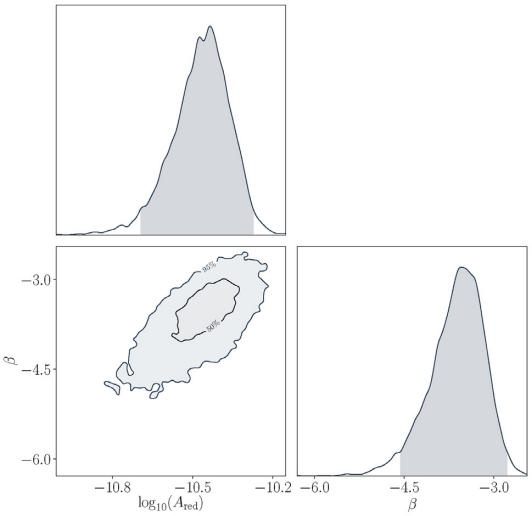

(a) Posterior distribution for PSR J0543+2329.

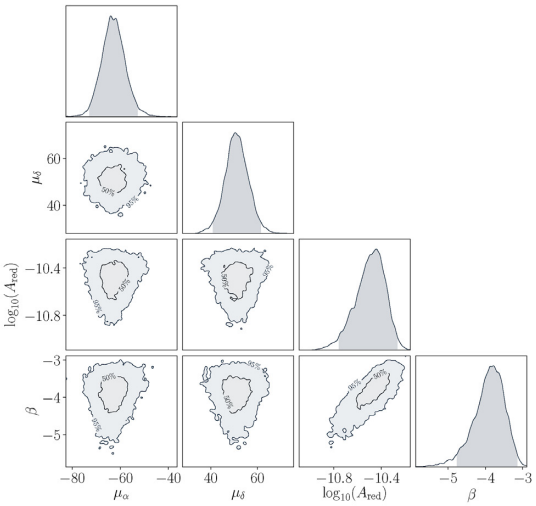

(b) Posterior distribution for PSR J0745-5353.

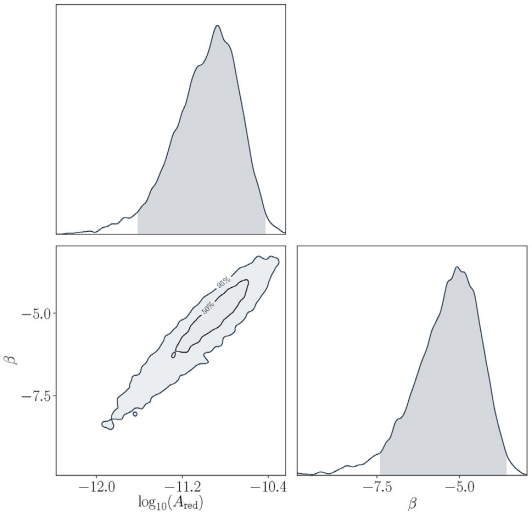

(c) Posterior distribution for PSR J0834-4159.

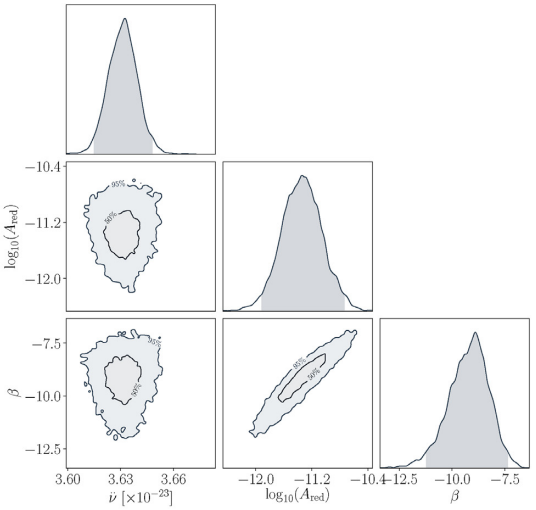

(d) Posterior distribution for PSR J0857-4424.

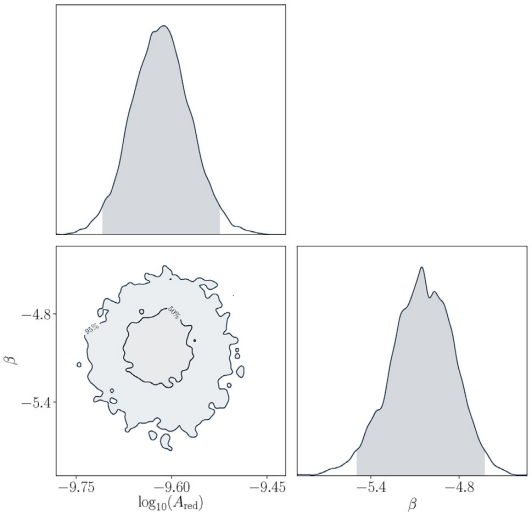

(e) Posterior distribution for PSR J0905-5127.

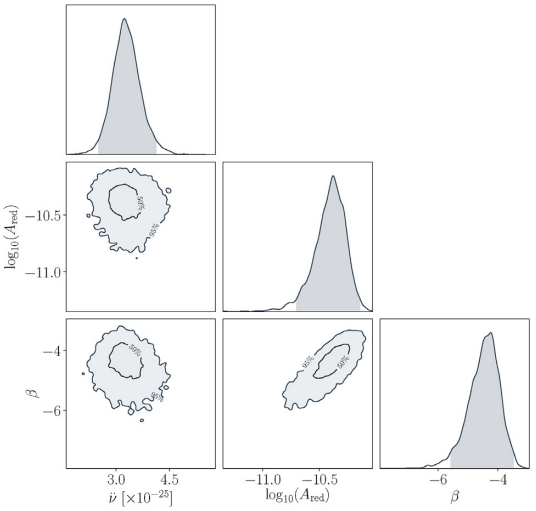

(f) Posterior distribution for PSR J0954-5430.

Figure A1. Sample posterior distributions of six pulsars. (a) Posterior distribution for PSR J0543+2329. (b) Posterior distribution for PSR J0745−5353. (c) Posterior distribution for PSR J0834−4159. (d) Posterior distribution for PSR J0857−4424. (e) Posterior distribution for PSR J0905−5127. (f) Posterior distribution for PSR J0954−5430.

This paper has been typeset from a TEX/LATEX file prepared by the author.